Bachelor's Thesis

**Czech
Technical
University
in Prague**

F3
Faculty of Electrical Engineering
Department of Control Engineering

Development of software for motor controller of an electric formula

Vojtěch Michal

Supervisor: Ing. Denis Efremov,
         doc. Ing. Tomáš Haniš, Ph.D
Field of study: Cybernetics and Robotics
May 2022

BACHELOR'S THESIS ASSIGNMENT

I. Personal and study details

Student's name: **Michal Vojtěch**   Personal ID number: **492355**

Faculty / Institute: **Faculty of Electrical Engineering**

Department / Institute: **Department of Control Engineering**

Study program: **Cybernetics and Robotics**

II. Bachelor's thesis details

Bachelor's thesis title in English:

Development of software for motor controller of an electric formula

Bachelor's thesis title in Czech:

Návrh řídicího software pro měnič pro elektrickou formuli

Guidelines:

The thesis aims to get familiar with the properties and control of three-phase permanent magnet synchronous motor (PMSM) and develop software for a silicon carbide (SiC) motor controller to be used in the international design competition Formula Student.
1) Study the characteristics of PMSM, including methods of control with emphasis on field oriented control.
2) Develop a mathematical model of formula's motors.
3) Design controller(s) for this model.
4) Implement motor controller's firmware in a low-level programming language (C++).
5) Verify design using simulations and real-world hardware.

Bibliography / sources:

[1] HAYES, John G. a Gordon A. GOODARZI. Electric powertrain: energy systems, power electronics and drives for hybrid, electric and fuel cell vehicles. Hoboken [NJ, USA]: Wiley, 2018. ISBN 9781119063643.
[2] FRANKLIN, G. F., POWELL, J. D., EMAMI-NAEINI, A. Feedback control of dynamic systems, Global Edition (7th edition). Pearson, 2015, ISBN 978-1-29-206890-9

Name and workplace of bachelor's thesis supervisor:

Ing. Denis Efremov   Department of Control Engineering FEE

Name and workplace of second bachelor's thesis supervisor or consultant:

doc. Ing. Tomáš Haniš, Ph.D.   Department of Control Engineering FEE

Date of bachelor's thesis assignment: **20.09.2021**   Deadline for bachelor thesis submission: **20.05.2022**

Assignment valid until:
by the end of summer semester 2022/2023

_____   _____   _____
Ing. Denis Efremov   prof. Ing. Michael Šebek, DrSc.   prof. Mgr. Petr Páta, Ph.D.
Supervisor's signature   Head of department's signature   Dean's signature

III. Assignment receipt

The student acknowledges that the bachelor's thesis is an individual work. The student must produce his thesis without the assistance of others, with the exception of provided consultations. Within the bachelor's thesis, the author must state the names of consultants and include a list of references.

_____   _____
Date of assignment receipt   Student's signature

Acknowledgements

Declaration

....
Vojtěch Michal
In Prague, 20. May 2022

Abstract

This bachelor's thesis aims to develop software for motor controller of an electric race car. Mathematical model of a Permanent Magnet Synchronous Motor (PMSM) is derived using concepts of space vectors with Clarke and Park transformations and fundamental physical laws governing the operation of rotating electrical machines.

Various motor control strategies, such as Field Oriented Control (FOC), and voltage modulation methods are reviewed. Tools of classical control theory are used to analytically find regulator gains for the parameterized motor model. System identification is discussed with emphasis on automated commissioning. The control algorithm is implemented on an STM32G474 microcontroller and theoretical results are verified in the laboratory environment.

Keywords: angle tracking observer, electric vehicle, field oriented control, system modelling, motor controller, permanent magnet synchronous motor, resolver

Supervisor: Ing. Denis Efremov, doc. Ing. Tomáš Haniš, Ph.D

Abstrakt

Tato bakalářská práce se zabývá návrhem řídicího systému frekvenčního měniče pro elektrický závodní vůz. Je odvozen matematický model synchronního motoru s permanentními magnety (PMSM) pomocí konceptu prostorových vektorů, Parkovy a Clarkové transformací a základních fyzikálních principů rotujících strojů.

Jsou srovnány různé strategie řízení motorů, například vektorové řízení (FOC), a metody modulace napětí. Pomocí postupů klasické teorie řízení jsou analyticky navrženy regulátory pro parametrizovaný model motoru. Je popsána identifikace systému s důrazem na identifikaci automatickou. Řízení je implementováno na mikrokontroleru STM32G474 pro ověření teoretických výsledků v laboratorním prostředí.

Klíčová slova: angle tracking observer, elektrické vozidlo, frekvenční měnič, modelování, resolver, synchronní motor s permanentními magnety, vektorové řízení

Překlad názvu: Návrh řídicího software pro měnič pro elektrickou formuli

Contents

Figures

Chapter 1

Introduction

Permanent magnet synchronous motor (PMSM) are characterized by their high efficiency, high power density and low maintenance costs. This makes them suitable for many applications, from tasks with predictable load such as pumps or fans to the highly dynamic environment of electric vehicles (EVs). Since PMSM is inherently an AC machine, a separate converter with semiconductor switches is typically required to convert supplied electrical energy to alternating current in a variable speed drive. Especially due to the advent of electromobility with battery-powered vehicles, precise and efficient motor control by the inverter has grown increasingly important.

These general requirements materialize in the environment of Formula Student – an international engineering competition for university students, revolving around design and manufacturing of a race car with either an internal combustion engine or electric powertrain. A well-established team of students from the Czech Technical University in Prague, Czech Republic, named *eForce FEE Prague Formula* takes part in the competition since its founding in 2010 and has built a dozen electric race cars, many of which enjoyed great achievements competing with students from other European countries.

This thesis aims to pick up the threads of the long-lasting tradition of in-house motor controller design in eForce. It concerns itself exclusively with the control algorithm and its implementation in low-level inverter firmware. Hardware design considerations are not addressed.

1.1 Motivation

Throughout the existence of *eForce FEE Prague Formula*, there have been two projects with the goal of designing a new inverter. The first custom motor controller was designed by Ing. Miroslav Rýzek during the 3rd season in 2013 and later improved in 2015, while the second motor controller was designed by Ing. Stanislav Tomášek in 2019. Although both colleagues fulfilled their goals, several criteria render their motor controllers unsuitable for upcoming generations of vehicles developed by eForce.

Both motor controllers were designed for tractive system voltages below 400 V, which have been replaced by 600 V tractive system for the last formula

generation. Ing. Rýzek's motor controller uses components that are nowadays classified as not recommended for new designs. Furthermore, the evolution of Formula Student competition rules rendered many aspects of his design no longer compliant, such as the software control of discharge circuitry, where only non-programmable hardware logic is permitted.

Several new components have since become available on the market, namely sillicon carbide (SiC) power MOSFETs and the STM32G4 family of microcontrollers. Ing. Tomášek's motor controller – design of which is described in his master's thesis [1] – was built around an intelligent power module *6MBP300VEA060-50* manufactured by *Fuji Electric*, incorporating actual semiconductor switches as well as necessary gate driver stage and various protections such as overcurrent and thermal. This high coupling of functionality meant that any attempt to design an inverter with SiC transistors would result in a complete device redesign.

The microcontroller STM32G474 – chosen for the implementation of all control algorithms – belongs to the STM32G4 family launched in 2019. Built around Cortex M4 core with floating point unit, it is suitable for digital signal processing. In addition to that, a rich set of on-chip peripherals allows the programmer to offload many tasks from the core. To highlight just a few important properties, the microcontroller contains five independent 12-bit analog to digital converters (ADC) with support for hardware oversampling, advanced and high resolution timers and two mathematical coprocessors – the *Filter Math Accelerator* (FMAC) for calculation of digital filters and CORDIC coprocessor for accelerated trigonometry. Especially the CORDIC coprocessor, further discussed in Section 7.2, is a game-changer in the motor control environment, allowing implementation of many algorithms, which would be computationally expensive when carried out in software.

A Formula Student vehicle has specific requirements, only partially incomparable with design requirements in customer automotive. Most importantly, with less than 200 kg excluding the pilot, extreme attention is paid to any excess weight. For this reason, among others, the currently used set of motor controllers *DCU60/60* manufactured by *Lenze Schmidhauser* – whose configuration for our use case is elaborated on in [2] – is not optimal. Combination of these reasons motivated a team of students to design a new motor controller from the ground up, learning from deficiencies of previous designs.

■ 1.2   Motor controller requirements

Permanent magnet synchronous motors used in the last generation of electric formula designed by eForce are manufactured by *Fischer Elektromotoren*, model *TI085-052-070-04B7S-07S04BE2*. Key datasheet parameters of this motor are listed in Table 1.1. They are expected to serve the team for several seasons due to their extraordinarily small size and high power output in comparison with motors utilized in previous seasons and, therefore, are considered the primary design target for the new motor controller.

For design of the control algorithm, other machine parameters, listed in

Parameter	Value
Nominal Torque	11.1 N m
Nominal Current	22.6 A
Peak Torque	29.1 N m
Peak Current	61 A
Peak Power	35.37 kW
Maximal Speed $n_{\max}$	20 kRPM

Table 1.1: Main parameters of Fischer PMSM.

Parameter	Value	Notes
Winding Connection		Star
Number of Polepairs n_{p}	4	
Maximal Electrical Frequency f_{e}	1333 Hz	$f_{\mathrm{e}} = n_{\mathrm{p}} n_{\max}/60$
Winding Resistance R	$0.126\,\Omega$	
Winding Inductance L	0.393 mH	
Electrical Time Constant τ_{e}	3.11 ms	$\tau_{\mathrm{e}} = L/R$
Torque Constant K_{t}	$0.492\,\mathrm{N\,m\,A^{-1}}$	
Speed Constant K_{e}	$0.296\,\mathrm{V\,s\,rad^{-1}}$	

Table 1.2: Parameters of Fischer PMSM relevant for the control algorithm.

Table 1.2 are important. Primarily the maximal electric frequency $f_{\mathrm{e}} = 1333\,\mathrm{Hz}$ dictates the lowest permissible switching frequency [3]

$$f_{\mathrm{s}} = 12 f_{\mathrm{e}} \approx 16\,\mathrm{kHz}. \tag{1.1}$$

To gain some safety margin, switching frequency $f_{\mathrm{s}} = 20\,\mathrm{kHz}$ has been chosen, which will also be the sampling frequency of all used discrete-time systems. Increasing the switching frequency further is not desirable, as switching losses are a linear function of switching frequency [4] and shorter switching period with constant dead time intervals causes growing distortion of voltage waveforms discussed in Section 3.2.

■ 1.3 Thesis structure

This thesis begins with an overview of mathematical tools widely used in the field of motor control. Two crucial linear mappings – Clarke and Park coordinate transformations – are formally derived using the concept of current space vectors and subsequently utilized to establish a mathematical model of PMSM by the end of Chapter 2. Chapter 3 investigates properties of several motor control strategies, arriving at the state-of-the-art Field Oriented Control algorithm. Thus are fulfilled guidelines (1) and (2) of the assignment and the reader is familiarized with the necessary background knowledge.

Chapter 4 tackles the important problem of rotor angle estimation. Suitable sensors are considered, putting emphasis on the benefits of the resolver. Sensorless methods are briefly mentioned for completeness. The chapter

continues with a discussion of resolver output demodulation, design of an angle tracking observer and concludes with its discretization and considerations of the implementation in software. Chapter 5 continues by exploring options to simplify motor mathematical model and designing controllers for it. Chapter 6 is concerned with identification of the controlled motor, focusing on automatic commissioning of the device. All three topics are accompanied by simulation and experimental data, proving the effectiveness of implemented procedures.

Chapter 7 highlights several key points of implementation on the actual hardware. The significance of mathematical coprocessors present in the microcontroller is underlined, enabling major performance improvements.

Chapter 2

Mathematical background

An ideal AC motor is assumed to have all phases of equal impedance[1] [3], and electrically equidistantly distributed along the machine geometry (i.e. the motor is assumed to be *symmetrical*). In the case of permanent magnet synchronous motor, the stator is composed of phase windings, whereas the rotor carries permanent magnets.

The general principle of operation is independent of the exact number of stator phases used, yet, for simplicity, only the three-phase configuration will be discussed further. Three is the minimum number of phases required to achieve two DOF and thus create a magnetic field rotating in plane. For this reason, the three-phase configuration is the most common and is used for all motors in eForce. To keep nomenclature consistent with the actual motor to be controlled, phases are labelled U, V and W.
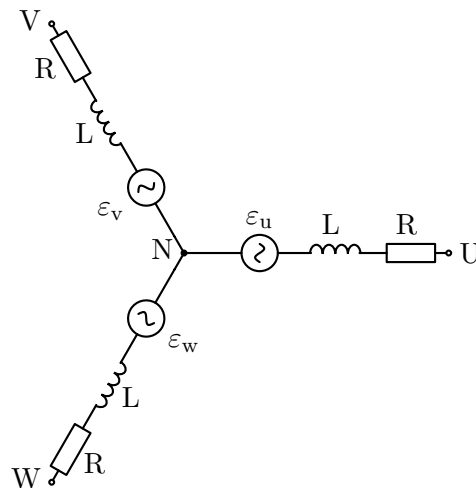
Figure 2.1: Equivalent schematic of a star-connected three-phase stator.

The stator is assumed to be connected in *star (wye) configuration* shown in Figure 2.1 with equal resistance R and inductance L of all windings, since this configuration lends itself to simpler mathematical modelling and is equivalent

---

[1]including both winding resistance and inductance, as well as mutual inductances from other windings

to the alternative *delta configuration*. Furthermore, due to the susceptibility of delta configuration to circulating third current harmonic, causing significant losses further analyzed in [5], the stator of targeted motors is in fact connected in star configuration. It is also beneficial to retain the concept of the star centre point being the *load neutral* point N. It serves as virtual ground of the machine, albeit not being directly accessible through motor terminals, and will be relied on heavily as a reference for phase voltages in later chapters. Comparison of star and delta stator configurations and their properties for machine operation are presented in [6].

2.1 Machine reference frames

Owing to its insightful approach, state-of-the-art technique for motor control is the *vector control* built around the concept of space vectors. Space vectors are used to represent values of machine quantities, such as voltage, current or magnetic flux linkage, embracing their spatial distribution [7]. Consider three phase currents i_u, i_v, and i_w as components of a vector $\vec{i} = \vec{e}_\mathrm{u} i_\mathrm{u} + \vec{e}_\mathrm{v} i_\mathrm{v} + \vec{e}_\mathrm{w} i_\mathrm{w} \in \mathbb{R}^3$ with canonical basis vectors $\vec{e}_k$ for $k = u, v, w$. Assuming that the *neutral point* N of the motor is not connected anywhere, phase currents are no longer linearly independent and the relation

$$i_\mathrm{u} + i_\mathrm{v} + i_\mathrm{w} = 0 \tag{2.1}$$

removes one degree of freedom. Such an AC system is called *balanced*. To simplify analysis and subsequent control, it is desirable to search for an alternative representation instead of the perspective of highly coupled phase variables. The following derivation is carried out for the machine current vector $\vec{i}$, it is however valid for other quantities, such as voltage $\vec{u} = \begin{bmatrix} u_\mathrm{u}, u_\mathrm{v}, u_\mathrm{w} \end{bmatrix}^T$ as well as flux linkage $\vec{\psi} = \begin{bmatrix} \psi_\mathrm{u}, \psi_\mathrm{v}, \psi_\mathrm{w} \end{bmatrix}^T$ (see Section 2.2.1) as well.[2]

2.1.1 Stator reference frame

Equation (2.1) describes a two dimensional linear subspace $P \subset \mathbb{R}^3$ – a plane – of all permissible[3] current vectors. An elementary result from linear algebra is the ability to choose various sets of vectors, whilst preserving their linear span. It is, therefore, possible to choose a different (non-canonical) orthonormal basis of $\mathbb{R}^3$, commonly labeled as $\alpha\beta0$, that aligns two of the three basis vectors $\vec{e}_\alpha, \vec{e}_\beta$ with plane P.

In order to have two basis vectors in a plane, the third one must be orthogonal to it, being a scaled normal. Interpreting the equation (2.1) as a

---

[2]page 26 first paragraph of [3]
[3]respecting the Kirchhoff current law
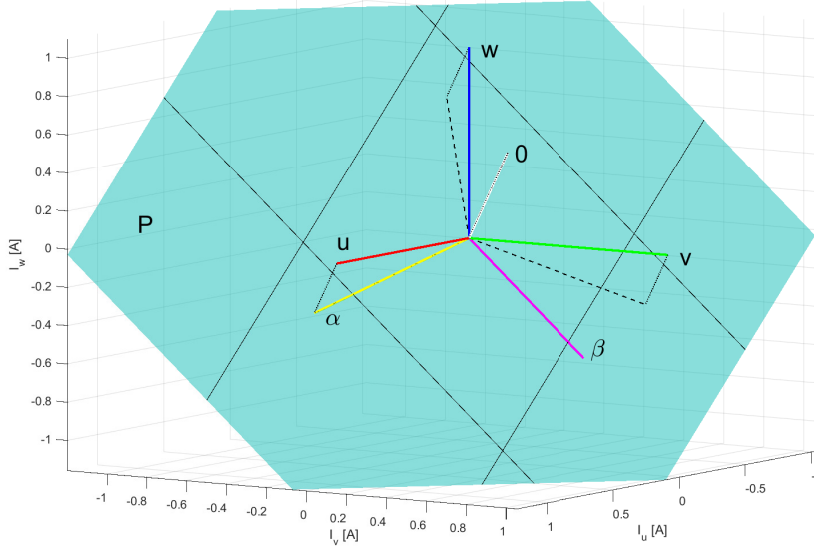
Figure 2.2: Coordinate systems uvw and $\alpha\beta0$ in $\mathbb{R}^3$ current space.

dot product of two orthogonal vectors, $\vec{e}_0$ can be chosen to be the unit vector

$$
\vec{e}_0 = \frac{1}{\sqrt{3}} \begin{bmatrix} 1 \\ 1 \\ 1 \end{bmatrix} = \sqrt{\frac{2}{3}} \begin{bmatrix} \frac{1}{\sqrt{2}} \\ \frac{1}{\sqrt{2}} \\ \frac{1}{\sqrt{2}} \end{bmatrix}. \tag{2.2}
$$

By convention, the first basis vector $\vec{e}_\alpha$ is chosen to be the orthogonal projection

$$
\vec{e}_\alpha = \frac{\vec{e}_u - \vec{e}_0 \cdot (\vec{e}_0^T \vec{e}_u)}{||\vec{e}_u - \vec{e}_0 \cdot (\vec{e}_0^T \vec{e}_u)||} = \sqrt{\frac{2}{3}} \begin{bmatrix} 1 \\ -\frac{1}{2} \\ -\frac{1}{2} \end{bmatrix} \tag{2.3}
$$

of $\vec{e}_u$ onto the plane P scaled to unity norm. The second basis vector $\vec{e}_\beta$ must be obtained from the cross product

$$
\vec{e}_\beta = \vec{e}_0 \times \vec{e}_\alpha = \sqrt{\frac{2}{3}} \begin{bmatrix} 0 \\ \frac{\sqrt{3}}{2} \\ -\frac{\sqrt{3}}{2} \end{bmatrix} \tag{2.4}
$$

to preserve the natural orientation of this coordinate frame.

From equations (2.2) through (2.4), a family of linear coordinate transformations between phase coordinates uvw and stator reference frame $\alpha\beta0$, known as *forward* and *inverse Clarke transformations*, are derived[4]. An illustration of both coordinate frames is given in Figure 2.2. Plane P is shown in

---

[4]Identical results can be alternatively derived by projecting $\vec{e}_u$, $\vec{e}_v$, $\vec{e}_w$ onto P yielding three vectors 120° disributed apart and then decomposing them into two orthogonal components using planar trigonometry.

7

cyan, elements of the canonical *uvw*-basis are drawn with red, green and blue, respectively. Yellow, magenta and while directions represent the alternative $\alpha\beta 0$ reference frame. For vectors that do not belong to P, the orthogonal projection onto P is drawn dashed and the corresponding orthogonal rejection is densely dotted.

Arranging the elements of $\alpha\beta 0$ basis as rows of a matrix yields the *power invariant Clarke transformation*

$$
\begin{bmatrix} i_\alpha \\ i_\beta \\ i_0 \end{bmatrix} = K \underbrace{\begin{bmatrix} 1 & -\frac{1}{2} & -\frac{1}{2} \\ 0 & \frac{\sqrt{3}}{2} & -\frac{\sqrt{3}}{2} \\ \frac{1}{\sqrt{2}} & \frac{1}{\sqrt{2}} & \frac{1}{\sqrt{2}} \end{bmatrix}}_{\mathbf{T}_{\mathrm{C,power}}} \begin{bmatrix} i_\mathrm{u} \\ i_\mathrm{v} \\ i_\mathrm{w} \end{bmatrix}, \quad \text{where } K = \sqrt{\frac{2}{3}}. \tag{2.5}
$$

Matrix $\mathbf{T}_{\mathrm{C,power}}$ is orthogonal[5], therefore the inverse transformation is given simply by the transpose $\mathbf{T}_{\mathrm{C,power}}^{T}$.

From the assumption of balanced system (2.1), one of phase currents can be expressed as a linear combination of others. Plugging $i_\mathrm{v} = -i_\mathrm{u} - i_\mathrm{w}$ into (2.5) yields

$$
\begin{bmatrix} i_\alpha \\ i_\beta \\ i_0 \end{bmatrix} = \mathbf{T}_{\mathrm{C,power}} \begin{bmatrix} i_\mathrm{u} \\ -i_\mathrm{u} - i_\mathrm{w} \\ i_\mathrm{w} \end{bmatrix} = \begin{bmatrix} \sqrt{\frac{3}{2}} i_\mathrm{u} \\ -\sqrt{2}(\frac{1}{2} i_\mathrm{u} + i_\mathrm{w}) \\ 0 \end{bmatrix}, \tag{2.6}
$$

from where two important observations can be made. First, it is apparent that the zero sequence component of $\alpha\beta 0$ frame is under stated assumptions always zero, hence carries no information and can be discarded from the transformation altogether[6]. This results in a *simplified* variant of Clarke transformation represented by a 2×3 or even 2×2 matrix, when one of the phase currents is left out.

Second, the power invariant transformation increases the amplitude of quantities by a factor of $\sqrt{\frac{3}{2}}$. The scaling factor may be adjusted to $K = \frac{2}{3}$, yielding the amplitude invariant form of forward Clarke transformation with unity gain. Since motor control relies on knowledge of amplitudes of machine currents and voltages, rather than power, only the simplified amplitude invariant transformation

$$
\begin{bmatrix} i_\alpha \\ i_\beta \end{bmatrix} = \frac{2}{3} \underbrace{\begin{bmatrix} 1 & -\frac{1}{2} & -\frac{1}{2} \\ 0 & \frac{\sqrt{3}}{2} & -\frac{\sqrt{3}}{2} \end{bmatrix}}_{\mathbf{T}_{\mathrm{C}}} \begin{bmatrix} i_\mathrm{u} \\ i_\mathrm{v} \\ i_\mathrm{w} \end{bmatrix} \tag{2.7}
$$

will be considered from this point. Although, strictly speaking, the matrix $\mathbf{T}_{\mathrm{C}}$ does not have an inverse, symbol $\mathbf{T}_{\mathrm{C}}^{-1}$ is used to denote the inverse transformation.

---

[5]i.e. nonsingular with column and rows forming orthonormal vector sets

[6]This fact is evident geometrically as well – when all meaningful vectors belong to a plane P, their component in the direction of P's normal is zero.
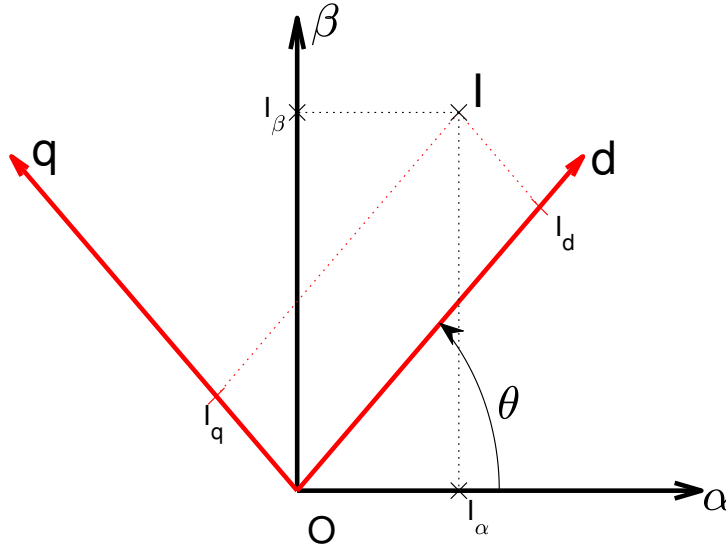
Figure 2.3: Coordinate systems $\alpha\beta$ and dq in $\mathbb{R}^2$.

■ 2.1.2 Rotor reference frame

The $\alpha\beta 0$ reference frame is fixed with respect to the stator. As the rotor turns, so do associated fields in the plane P. An alternative perspective is offered by rotating the stator frame about the zero sequence axis synchronously with the rotation of the motor. The $dq0$ reference frame, also called synchronous reference frame, is fixed to the rotor magnetic flux and thus converts rotating vectors representing AC quantities into stationary vectors representing DC quantities. Using the same argument as in Section 2.1.1, zero sequence component orthogonal to the plane of interest P can be omitted.

The linear mapping

$$\begin{bmatrix} i_d \\ i_q \end{bmatrix} = \underbrace{\begin{bmatrix} \cos\theta_{\mathrm{e}} & -\sin\theta_{\mathrm{e}} \\ \sin\theta_{\mathrm{e}} & \cos\theta_{\mathrm{e}} \end{bmatrix}}_{\mathbf{T}_{\mathrm{P}}(\theta_{\mathrm{e}})} \begin{bmatrix} i_\alpha \\ i_\beta \end{bmatrix}, \tag{2.8}$$

between $\alpha\beta$ and dq reference frames, illustrated in Figure 2.3, is called the *(forward) Park transformation*. It is a simple clockwise rotation by an immediate electrical angle θ_{e}. Various authors differ in terminology, whether the Park transformation maps to dq from $\alpha\beta$ (rotation only) or from uvw (rotation preceded by Clarke transformation) reference frames (e.g. [8]).

This approach significantly simplifies various aspects of system control. Among others, sinusoidal setpoints are replaced by steps and ramps.

9

2.1.3 Use of zero sequence component

A note should be made regarding the validity of assumption (2.1). It is indeed possible for the current vector $\vec{i}$ to leave the plane P in Figure 2.2. For example, stray capacitance is present between the motor case and the load neutral point N. As the potential of N is not constant but rather changes with the common-mode component of phase voltages – which is zero for standard sinusoidal modulation but non-zero for SVM or sinusoidal modulation with injected third harmonic – the stray capacitance is periodically (dis)charged, causing a small zero sequence current to flow. Nevertheless, its effects are – from the motor control point of view – negligible.

Second, zero sequence current flows in case of failures, namely due to a failure of insulation between windings and the motor case. Such a condition is a severe safety concern and possible cause of device damage and – more importantly – human injury. For this reason, the magnitude of the zero component may be calculated in real-time in order to detect unwanted alternative return paths for the current.

Implementation of this mechanism requires measurement of all three phase currents, instead of measuring two and calculating the third, hence increasing design complexity and cost. To truly mitigate the threat of damage or injury due to insulation failure in a real application, systems are equipped with a dedicated insulation monitoring device. Principle of IMD's operation is explained in [9].

2.2 Motor modelling

Although various types of motors differ greatly in mechanical construction or tasks they are built to handle, underlying physical principles are shared. In this section, several laws of physics are reviewed, forming a basis for the subsequent explanation of simple DC motor operation. From there, the PMSM is analyzed using coordinate transformations developed in Sections 2.1.1 and 2.1.2 in order to arrive at a simple mathematical model resembling the DC machine.

2.2.1 Physics of a rotating machine

The Lorentz force

$$\vec{F} = q(\vec{E} + \vec{v} \times \vec{B}) \tag{2.9}$$

describes the combined force exerted by an electric field with intensity $\vec{E}$ and a magnetic field with density $\vec{B}$ on a particle with charge q moving with velocity $\vec{v}$.

All charged particles enclosed in a wire carrying current I have nonzero mean drift velocity, making them subject to (2.9) when a magnetic field $\vec{B}$ is applied externally. Invoking the principle of superposition, individual

microscopic forces add up to produce a macroscopic force

$$\vec{F} = Q\vec{v} \times \vec{B} = \frac{\mathrm{d}}{\mathrm{d}t}\vec{l}Q \times \vec{B} = I\vec{l} \times \vec{B} \qquad (2.10)$$

experienced by the conductor. The $q\vec{E}$ component always points in the direction of flow inside the conductor and does not contribute to the electromagnetic torque of the machine [7].

Second, according to the Maxwell-Faraday equation

$$\vec{\nabla} \times \vec{E} = -\frac{\partial \vec{B}}{\partial t}, \qquad (2.11)$$

changing magnetic field influences the electric field and vice versa. Assuming a conductive loop $\partial\Sigma$ enclosing a surface Σ, both sides of (2.11) may be integrated over Σ yielding the integral form of (2.11)

$$\oint_{\partial\Sigma} \vec{E} \cdot \mathrm{d}\vec{l} = -\frac{\mathrm{d}}{\mathrm{d}t} \iint_{\Sigma} \vec{B} \cdot \mathrm{d}\vec{S}, \qquad (2.12)$$

where the Stokes theorem has been invoked on the left hand side, converting the surface integral of rotation into a contour integral along the surface border. Observing that

1. voltage u – a difference of electric potentials at points A and B – is defined as the contour integral of electric intensity $\vec{E}$ along a curve from B to A, and

2. the surface integral on the right hand side of (2.12) is the definition of magnetic flux Φ penetrating the surface Σ,

the standard form of Faraday's law of induction

$$u_{\mathrm{emf}} = -\frac{\mathrm{d}}{\mathrm{d}t}\Phi \qquad (2.13)$$

can be readily derived. The induced voltage – also called *electromotive force* – is usually labelled ε, yet in order to underline connection with the major manifestation of (2.13) in a rotating machine, i.e. the BEMF voltage measurable between armature circuit terminals when the motor is spun, no new symbol is introduced.

An extension of magnetic flux Φ for a coil with N turns is the *flux linkage*

$$\psi(t) = Nk_{\mathrm{w}}\Phi(t) = Li(t), \qquad (2.14)$$

where k_{w} is the winding factor, a constant for the given coil incorporating small imperfections, such as the variance in flux linked by each individual turn [10]. The flux linkage is sometimes labelled λ in other literature, e.g. [4], [11]. A coil generates a magnetic field with flux linkage $\psi(t)$ directly proportional to the instantaneous magnetizing current $i(t)$ with a constant of proportionality L – the coil *self-inductance*. *Mutual inductance* M then describes the flux linkage generated by one winding in response to current flowing through another.

11
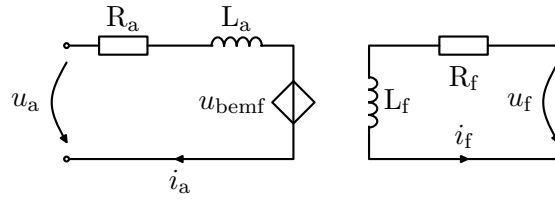
Figure 2.4: Electrical schematic of a separately excited DC machine.

2.2.2 Model of a DC machine

The simplest possible design of a DC motor is a loop – the so-called *armature* – of area S located between two magnets. Assuming the magnetic field is homogenous[7], the definition of magnetic flux simplifies to

$$\Phi = BS \cos \alpha, \tag{2.15}$$

where α is the angle between $\vec{B}$ and loop normal. Applying voltage between armature terminals causes current I to flow, producing force (2.10). Since the current flows in an opposite direction when returning from the machine, forces acting on either side of the loop are equal in magnitude and have opposite direction. When the loop is allowed to rotate freely, the produced electromagnetic torque attempts to align it with $\vec{B}$, such that $\alpha = \frac{\pi}{2}$, hence $\Phi = 0$ and forces acting on both forward and return paths cancel out. At that point, the system enters stable equilibrium and does not move anymore.

Commutator action is required for continuous rotation – as the loop passes through position $\alpha = \frac{\pi}{2}$, the resultant torque is zero, allowing the system to overshoot due to accumulated kinetic energy and enter damped oscillations around the equilibrium, until excess energy is dissipated through losses, especially friction. However, if the direction of current is suddenly reversed, the new resultant torque forces the loop to rotate further in the same direction. Reversing[8] the direction of current twice every mechanical revolution causes the motor to rotate.

In a separately excited DC machine – schematic of which is displayed in Figure 2.4 – the homogenous magnetic field is no longer generated by permanent magnets, but rather by current i_f flowing through an additional *field winding*. From the perspective of the control theory, a separately excited DC motor in the electrical domain consists of a first-order armature system with state i_a connected to the mechanical domain through a gyrator, whose modulus is proportional to the field winding current i_f – the state of the other first-order system. Behaviour of this system in the electrical domain is

---

[7]i.e. $\vec{B}$ constant everywhere in the air gap
[8]either in the power supply or using a mechanical commutator

governed by equations [12]

$$u_\mathrm{f} = R_\mathrm{f} i_\mathrm{f} + L_\mathrm{f} \frac{\mathrm{d}}{\mathrm{d}t} i_\mathrm{f},$$
$$u_\mathrm{a} = R_\mathrm{a} i_\mathrm{a} + L_\mathrm{a} \frac{\mathrm{d}}{\mathrm{d}t} i_\mathrm{a} + u_\mathrm{bemf}, \tag{2.16}$$
$$u_\mathrm{bemf} = K_1(i_\mathrm{f}) \omega_\mathrm{m},$$
$$T_\mathrm{e} = K_2(i_\mathrm{f}) i_\mathrm{a},$$

where $K_{1,2}(i_\mathrm{f})$ are moduli of the gyrator, usually labeled the *motor constant* and the *torque constant*, respectively. For energy to be conserved, $K_1 = K_2^{-1}$ must be satisfied when converted to base units. Scaling factors are applied in practice to account for different units, namely the use of RPM instead of rad/s to express mechanical angular speed ω_m.

■ 2.2.3 Mechanical dynamics

Mechanical dynamics of a motor producing electromagnetic torque T_e and rotating with mechanical speed ω_m are governed by the equation of motion [8]

$$J \frac{\mathrm{d}}{\mathrm{d}t} \omega_\mathrm{m} + b\, \omega_\mathrm{m} = T_\mathrm{e} - T_\mathrm{load}, \tag{2.17}$$

where J is the moment of inertia, b is the coefficient of friction and T_load represents torque from the load, which may be non-zero for non-passive loads such as a brake. Connecting the motor shaft to a gearbox results in (ideally) constant b, whereas J varies greatly with operating conditions.

Due to a comparably greater time constant $\tau_\mathrm{m} = J/b$, mechanical dynamics are significantly slower than the electrical and therefore neglected. The angular frequency ω_m can thus be assumed to be a quasi-constant parameter [13].

■ 2.2.4 Mechanical and electrical angles

In practice, motors have multiple pairs of magnets and corresponding phase windings – among others in order to smoothen the generated torque and induced voltage [11] – rather than only two as assumed in the analysis above. This assumption, however, does not devalue achieved results, as the actual number of poles does not influence machine's electrical properties in any way [7]. All magnets are distributed regularly along the entire rotor circumference, alternating between south and north pole, together forming n_p pole pairs. Magnetic poles always come in pairs and – obviously – there may not be less than one pole pair in a motor, therefore

$$n_\mathrm{p} \geq 1, \quad n_\mathrm{p} \in \mathbb{N}. \tag{2.18}$$

Mechanical rotation by a whole number of pole pairs leaves the rotor in an electrically indistinguishable state – the electrical domain exhibits a rotational

symmetry of order n_p – and therefore the electrical angle

$$\theta_\mathrm{e} = n_\mathrm{p}\theta_\mathrm{m} \tag{2.19}$$

is a linear function of mechanical angle θ_m. Repeated differentiation of (2.19) with respect to time yields similar linear relations for angular frequency and angular acceleration.

In this thesis, angles are given in radians unless indicated otherwise. For angular speed, an alternative and more intuitive unit are the *revolutions per minute* (RPM), in which case the speed is often labelled n and can be expressed as

$$n = 60f_\mathrm{m} = \frac{60}{n_\mathrm{p}}f_\mathrm{m} = \frac{30}{\pi n_\mathrm{p}}\omega_\mathrm{e}, \tag{2.20}$$

where $f_\mathrm{m} = \frac{\omega_\mathrm{m}}{2\pi}$ and $f_\mathrm{e} = n_\mathrm{p}f_\mathrm{m}$ are the mechanical and electrical frequency, respectively.

■ 2.2.5 Structure of a PMSM

Starting from a DC machine with permanent magnets on the stator, the role of stator and rotor can be swapped – mounting permanent magnets on the rotor and using stator as the armature – to arrive at the principle of PMSM's operation [4]. Since mechanical commutation is no longer possible, it must be replaced by an electronic one, utilizing semiconductor switching elements.

The placement of permanent magnets on the machine's rotor is the simplest criterion for classification of PMSM. In a *surface mount* PMSM (SMPMSM), magnets are placed on the round rotor, extending into the air gap. On the other hand, in the case of the *interior* PMSM (IPMSM), permanent magnets are placed inside the rotor. This increases mechanical robustness and removes the danger of PMs being torn off of the rotor during high speed operation, but comes at a cost of reduced flux density in the air gap. An exhausting description of various PMSM topologies and their key properties is given in [14].

The direct axis d is by definition aligned with the flux of permanent magnets, while the quadrature axis q is electromagnetically orthogonal to it. An illustration of the relation of dq reference frame to actual PMSM rotor construction is in Figure 2.5. There is a difference in relative permeability μ_r of permanent magnets ($\mu_\mathrm{r} \approx 1$) and iron (μ_r in order 10^3). This causes a significant difference between IPMSM and SMPMSM rotor from the perspective of magnetic reluctance $\mathcal{R}$ – for an interior magnet PMSM each PM can be thought of as a cut into the rotor, extending the air gap along the d axis and increasing reluctance, whereas along the q axis no change in reluctance is observed. Therefore $\mathcal{R}_\mathrm{d} > \mathcal{R}_\mathrm{q}$ and [4]

$$L_\mathrm{d} < L_\mathrm{q}. \tag{2.21}$$

To quantify the difference between d and q axis inductances, dimensionless quantity *saliency* is defined as

$$\rho = \frac{L_\mathrm{q}}{L_\mathrm{d}}. \tag{2.22}$$

14
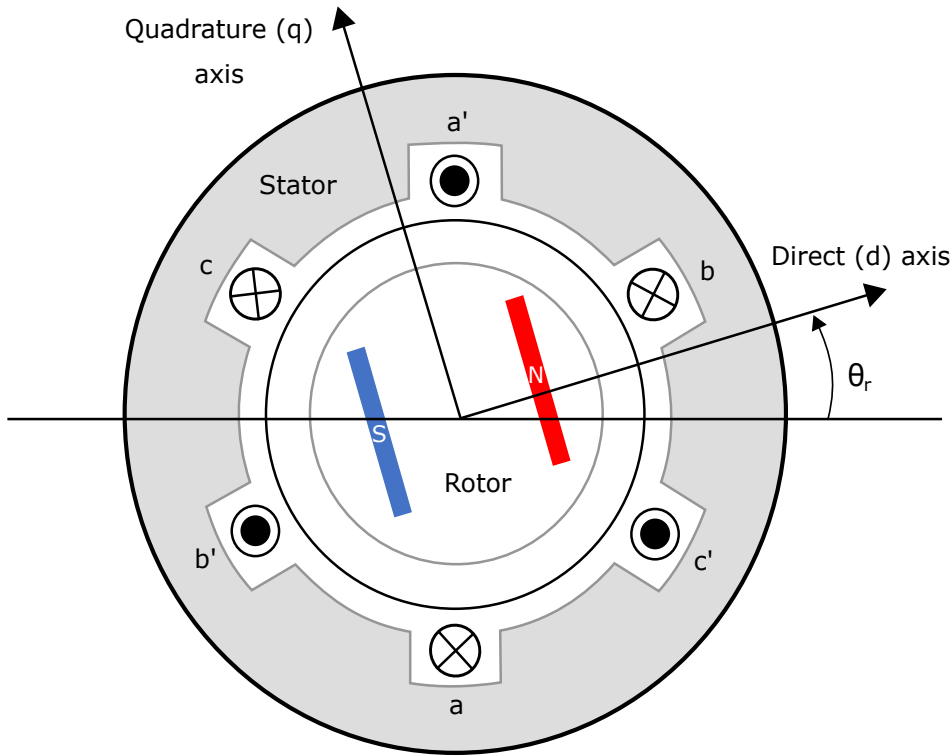
Figure 2.5: Alignment of *dq* reference frame with respect to rotor flux, from[15].

Similar behaviour is negligible in a SMPMSM since permanent magnets are located in the air gap, rather than inside the rotor, not causing a significant difference in inductance (therefore $\rho \approx 1$, while for IPMSM e.g. $\rho = 3$ or more).

Stator windings are assumed to be sinusoidally distributed along the machine geometry. The alternative concentrated winding – typical for BLDC motors – produces trapezoidal BEMF and undesirable cogging torque at low speeds, unless compensated for. Overview and comparison of both winding designs are presented in [16].

▪ 2.2.6 Model of a PMSM with sinusoidal BEMF

To derive the PMSM model, the usual assumptions of negligible magnetic saturation and eddy currents are made [8]. First, using the properties of a balanced star connected stator, three phase windings illustrated in Figure 2.1 and highly coupled machine quantities in the *uvw* frame are replaced by a perspective of the stator reference frame $\alpha\beta$ with two independent windings, as shown in blue in Figure 2.6. Kirchhoff's voltage law yields an equation for voltage across each winding

$$
\begin{aligned}
u_\alpha &= R_{\mathrm{s}} i_\alpha + \frac{\mathrm{d}}{\mathrm{d}t} \psi_\alpha, \\
u_\beta &= R_{\mathrm{s}} i_\beta + \frac{\mathrm{d}}{\mathrm{d}t} \psi_\beta,
\end{aligned}
\tag{2.23}
$$
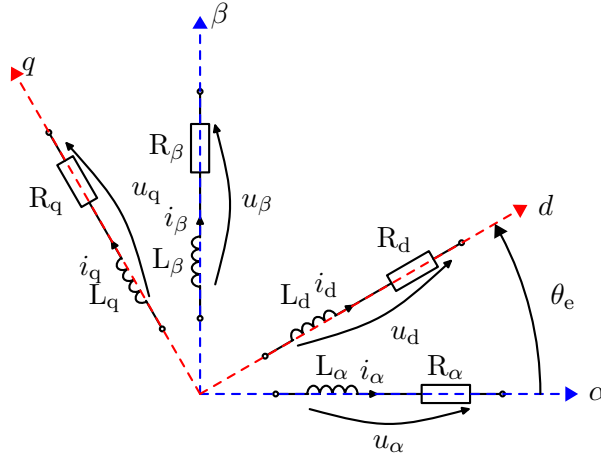
Figure 2.6: Pairs of independent windings in the $\alpha\beta$ (in blue) and dq (in red) reference frames.

where each flux linkage is composed of several terms. In the case of α axis flux linkage

$$\psi_\alpha = \underbrace{L_\alpha i_\alpha}_{A} + \underbrace{M i_\beta}_{B} + \underbrace{\psi_M \cos\theta_e}_{C}, \tag{2.24}$$

these terms are

- a self-inductance term (A) proportional to current i_α flowing through α axis winding,

- a mutual inductance term (B) proportional to current i_β in the β axis winding, and

- a projection term (C) of flux linkage of PM ψ_M into the α axis.

Equation for ψ_β is symmetrical to (2.24). Mutual inductances M and winding resistances R_s are assumed to be equal due to the symmetry of machine geometry [4].

It is apparent from (2.23) and (2.24) that voltages accross windings in the $\alpha\beta$ frame depend on the instantaneous electrical angle θ_e and so do inductances $L_{\alpha,\beta}$ due to manifestation of saliency discussed above. Although it is possible to express PMSM differential equations in the *uvw* or $\alpha\beta$ reference frames, as demonstrated in [4], transformation to *dq* frame – by definition rotating synchronously with the rotor magnetic flux ψ_{PM} and hence transforming all rotor angle dependent quantities to constants – using Park transform (2.8) simplifies the process enormously.

Replacement of real machine windings by a pair of virtual windings along the *d* and *q* machine axes, as illustrated in red in Figure 2.6, yields equations

16

[4]

$$u_{\mathrm{d}} = R_{\mathrm{s}}i_{\mathrm{d}} + \frac{\mathrm{d}\psi_{\mathrm{d}}}{\mathrm{d}t} - \omega_{\mathrm{e}}\psi_{\mathrm{q}},$$

$$u_{\mathrm{q}} = R_{\mathrm{s}}i_{\mathrm{q}} + \frac{\mathrm{d}\psi_{\mathrm{q}}}{\mathrm{d}t} + \omega_{\mathrm{e}}\psi_{\mathrm{d}}, \tag{2.25}$$

$$\psi_{\mathrm{d}} = L_{\mathrm{d}}i_{\mathrm{d}} + \psi_{\mathrm{M}},$$

$$\psi_{\mathrm{q}} = L_{\mathrm{q}}i_{\mathrm{q}}.$$

independent of instantaneous rotor angle. The flux linkage of permanent magnets now only contributes to the *d* axis. Expanding and rearranging (2.25) gives a non-linear state-space model of PMSM in the electrical domain [4], [8], [14], [17]

$$\frac{\mathrm{d}}{\mathrm{d}t}i_{\mathrm{d}} = \frac{1}{L_{\mathrm{d}}}(-R_{\mathrm{s}}i_{\mathrm{d}} + u_{\mathrm{d}} + \omega_{\mathrm{e}}L_{\mathrm{q}}i_{\mathrm{q}}),$$

$$\frac{\mathrm{d}}{\mathrm{d}t}i_{\mathrm{q}} = \frac{1}{L_{\mathrm{q}}}(-R_{\mathrm{s}}i_{\mathrm{q}} + u_{\mathrm{q}} - \omega_{\mathrm{e}}(L_{\mathrm{d}}i_{\mathrm{d}} + \psi_{\mathrm{M}})). \tag{2.26}$$

This model will be used as a basis for the subsequent design of controllers in Chapter 5. An alternative form [13]

$$\begin{bmatrix} u_{\mathrm{d}} \\ u_{\mathrm{q}} \end{bmatrix} = \underbrace{\begin{bmatrix} R_{\mathrm{s}} + L_{\mathrm{d}}s & -\omega_{\mathrm{e}}L_{\mathrm{q}} \\ \omega_{\mathrm{e}}L_{\mathrm{d}} & R_{\mathrm{s}} + L_{\mathrm{q}}s \end{bmatrix}}_{\mathbf{Z}} \begin{bmatrix} i_{\mathrm{d}} \\ i_{\mathrm{q}} \end{bmatrix} + \underbrace{\begin{bmatrix} 0 \\ \omega_{\mathrm{e}}\psi_{\mathrm{M}} \end{bmatrix}}_{\vec{u}_{\mathrm{bemf}}} \tag{2.27}$$

is acquired through the application of the Laplace transform on (2.25) under the assumption of zero initial conditions and rearrangement into matrix form. This form enables an intuitive observation, decomposing the motor equation into an impedance matrix $\mathbf{Z}$ and the rotational BEMF voltage $\vec{u}_{\mathrm{bemf}}$.

The PMSM model after transformation to the *dq* reference frame resembles the separately excited DC machine model (2.16). Both axes are independent, except for cross-coupling terms with ω_{e}, a manifestation of mutual inductance M present between windings. Authors of [17] show that the gyrator modulus in (2.16) is exactly the flux of PM in a PMSM. From (2.21) follows that the *d* axis system has time constant greater or equal to that in the *q* axis, assuming equal stator resistances R_{s}.

■ Power and torque of PMSM

The three-phase instantaneous power is

$$p_{uvw} = \vec{u}_{\mathrm{uvw}}^T \vec{i}_{\mathrm{uvw}} = u_{\mathrm{u}}i_{\mathrm{u}} + u_{\mathrm{v}}i_{\mathrm{v}} + u_{\mathrm{w}}i_{\mathrm{w}}. \tag{2.28}$$

Substituting

$$\vec{u}_{uvw} = \mathbf{T}_{\mathrm{C}}^{-1}\mathbf{T}_{\mathrm{P}}^{-1}\vec{u}_{dq},$$

$$\vec{i}_{uvw} = \mathbf{T}_{\mathrm{C}}^{-1}\mathbf{T}_{\mathrm{P}}^{-1}\vec{i}_{dq}, \tag{2.29}$$

where $\mathbf{T}_{\mathrm{P}}^{-1}$ and $\mathbf{T}_{\mathrm{C}}^{-1}$ are the inverse Park and Clarke transforms, respectivelly, into (2.28) yields a formula for instantaneous electric power

$$p_{\mathrm{e}} = \frac{3}{2}(u_{\mathrm{q}}i_{\mathrm{q}} + u_{\mathrm{d}}i_{\mathrm{d}}) = \frac{3}{2}\vec{u}_{\mathrm{dq}}^T \vec{i}_{\mathrm{dq}} \tag{2.30}$$

17

in the rotating reference frame [4], [8].

Substituting for voltages $\vec{u}_{\mathrm{dq}}$ in (2.30) from (2.25), power in the electrical domain

$$p_{\mathrm{e}} = \frac{3}{2}\left(R_{\mathrm{s}}\left(i_{\mathrm{q}}^2 + i_{\mathrm{d}}^2\right) + \left(L_{\mathrm{q}}i_{\mathrm{q}}si_{\mathrm{q}} + L_{\mathrm{d}}i_{\mathrm{d}}si_{\mathrm{d}}\right) + \omega_{\mathrm{e}}i_{\mathrm{q}}\left(\psi_{\mathrm{M}} + \left(L_{\mathrm{d}} - L_{\mathrm{q}}\right)i_{\mathrm{d}}\right)\right)$$
(2.31)

can be decomposed into several components. The first two terms represent energy dissipated into heat through resistive losses and energy exchanged with the magnetic field. The last term describes the power transferred through the air gap into the mechanical domain. Invoking the principle of conservation of energy, the mechanical power is

$$p_{\mathrm{m}} = \omega_{\mathrm{m}}T_{\mathrm{e}} = \omega_{\mathrm{e}}i_{\mathrm{q}}\left(\psi_{\mathrm{M}} + \left(L_{\mathrm{d}} - L_{\mathrm{q}}\right)i_{\mathrm{d}}\right). \tag{2.32}$$

Cancelling the angular frequency from both sides of the equation, a closed-form expression for generated electromagnetic torque [8], [18]

$$\begin{aligned} T_{\mathrm{e}} &= \frac{3}{2}n_{\mathrm{p}}i_{\mathrm{q}}\left(\psi_{\mathrm{M}} + i_{\mathrm{d}}\left(L_{\mathrm{d}} - L_{\mathrm{q}}\right)\right) \\ &= \frac{3}{2}n_{\mathrm{p}}i_{\mathrm{q}}\left(\psi_{\mathrm{d}} - i_{\mathrm{d}}L_{\mathrm{q}}\right) \end{aligned} \tag{2.33}$$

can be readily derived. For a non-salient motor (saliency ratio $\rho \approx 1$) or zero direct axis current $i_{\mathrm{d}} = 0$, equation (2.33) simplifies to

$$T_{\mathrm{e}} = \underbrace{\frac{3}{2}n_{\mathrm{p}}\psi_{\mathrm{M}}}_{K_t}\,i_{\mathrm{q}}, \tag{2.34}$$

where K_t is the torque constant of the motor.

■ 2.2.7 Other motor topologies

Aside from PMSM, other motor topologies include AC induction machines, brushless DC motors (BLDC) or reluctance motors. The already discussed DC motor is the simplest machine, making it suitable especially for low power and low cost applications, e.g. toys or small fans. Elimination of the mechanical commutator is desirable, as it is the primary cause of internal friction losses [17] and its maintenance implies machine downtime [8]. Only a brief overview of the key properties of individual motors is presented in this thesis. Elaborate materials on this topic include [7], [10].

In an AC induction motor, the stator must first induce current into the rotor for flux to be generated. This requires non-zero *slip* – the relative difference between the *synchronous speed* of the stator electric field and the *operating speed* of the rotor – to generate torque.[9] Brushless DC motor (BLDC) is similar to PMSM in both construction and principle of operation, windings of

---

[9]With zero slip (synchronous rotation of the rotor and the stator field), the rotor experiences no time change of Φ and hence no torque generating current is induced.

its phases are, however, not sinusoidally distributed but rather concentrated, generating trapezoidal BEMF. The reluctance motor has the simplest rotor structure, free of any permanent magnets. It is spatially organized to maximize magnetic saliency and thus create a single low reluctance path for the flux of the stator. As a consequence, the rotor "prefers" alignment with the stator to minimize system energy and thus synchronously follows its rotation [11]. The omission of permanent magnets completely eliminates the greatest reliability concern with PMSM – the Curie temperature of permanent magnets, at which the alignment of individual magnetic domains is shattered, resulting in complete loss of magnetic properties.

Chapter 3

Motor control

This chapter starts with a short overview of various control strategies for motors described in Section 1.2. Field Oriented Control is chosen as the most suitable strategy to fulfil design requirements. The end of this chapter is concerned with various voltage modulation strategies, especially the state-of-the-art *space vector modulation* and sinusoidal modulation with injected third harmonic. Regulator design is postponed until Chapter 5, estimation of angular position until Chapter 4.

3.1 Motor control strategies

3.1.1 Scalar control

Scalar control is used primarily for AC induction machines. Under the assumption of negligible voltage drop over winding resistance, the voltage u applied across motor terminals – now mostly composed of BEMF voltage – is proportional to rotor flux Φ and frequency of rotation f [19]. If the flux Φ and hence torque is to be left constant, this relation can be rearranged to

$$\frac{u}{f} = \text{const},\tag{3.1}$$

giving the method its alternative name "U/f" or "V/F". At low speed, when BEMF contributes only to a part of u and the controller applied voltage must take the increased impact of resistive losses into account and compensate it [11].

The simplicity of this strategy comes at a cost of poor dynamic performance [20]. It is by nature an open-loop technique, in which case its accuracy suffers since the machine slip is not known. By measuring shaft speed and closing a control loop around it, the accuracy and as well as the dynamic performance can be improved [20]. Utilization of scalar control for PMSM is not impossible, as presented in [21], especially for applications with predictable load and slow dynamics, such as pumps, fans or compressors. It is, however, not appropriate for precise control of generated torque, rendering it unsuitable for employment in EV drivetrain.
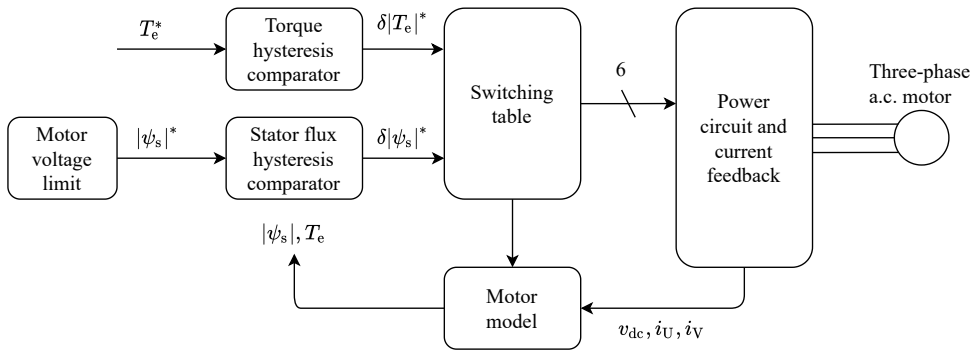
Figure 3.1: Block diagram of DTC, from [11], Figure A4.41.

3.1.2 Direct torque control

Direct torque control (DTC) is a method of vector attempting to decouple machines flux and torque and control then independently. Originally introduced for AC induction machines, the DTC was optimized for hardware implementation. Rather than using dynamic regulators of current and voltage are used in conjunction with the machine model to estimate the instantaneous torque and flux. Both quantities are fed into hysteresis controllers and a lookup table of switching combinations for each possible scenario[1] decides on the driving signals for switching components. The block diagram of this algorithm is shown in Figure 3.1.

As pointed out in [22], the conventional DTC has poor dynamic performance with significant torque ripple even at the steady state. Furthermore, the naive implementation is characterized by variable switching frequency, although there are methods to address this drawback, such as in [23].

3.1.3 Field oriented control

Field oriented control does not attempt to control the machine torque and magnetic flux directly, but rather indirectly through controlling currents in the *dq* reference frame. First, making use of the instantaneous electrical angle θ_e, measured phase currents $\vec{i}_{uvw}$ are transformed to the rotor reference frame, where regulation of $\vec{i}_{dq}$ takes place. The controller outputs voltage $\vec{u}_{dq}$, which is fed into the modulator to produce driving signals for individual semiconductor switches. Simplified block diagram of this control strategy is depicted in Figure 3.2. The actual structure of both the modulator and the controller may be experimented with, as the defining property of this strategy is the decoupling of currents in *d* and *q* axes.

The design of the modulator is discussed in Section 3.2. Both coordinate transformations, as well as the model of the controlled machine, have already been derived in Chapter 2. The feedback block labelled "Resolver & ATO" is responsible for shaft angle estimation and is elaborated on in Chapter 4.

---

[1]Tuple of the electrical sector for space vector modulation, and requests to increase, hold or decrease flux or torque
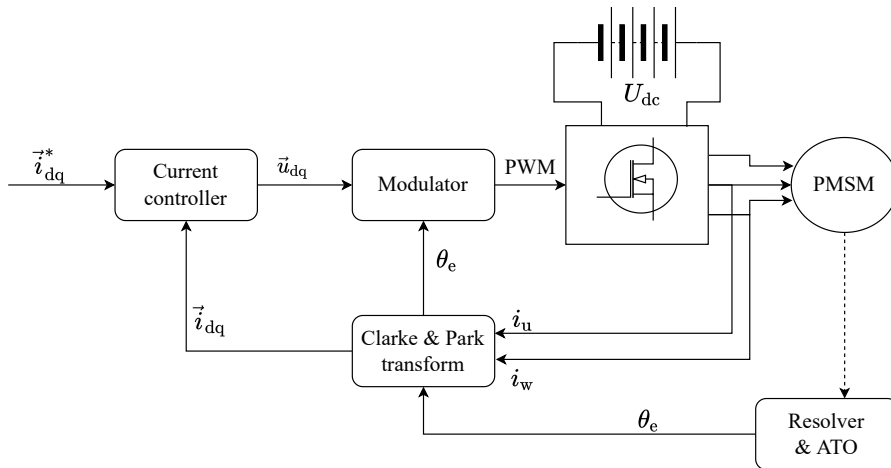
Figure 3.2: Block diagram of FOC

The typical controller structure used along with FOC is cascaded with PI regulators – an inner loop running at the highest sampling frequency (up to the transistor switching frequency f_s) is responsible for the control of current and therefore machine torque. Around that, a slower outer speed loop is closed, whose outputs serve as inputs to the current loop.

In the intended application of an electric race car designed by eForce, the motor controller is not concerned with control of speed. A dedicated electronic control unit, called the *Vehicle Dynamics Control Unit* and abbreviated VDCU, is responsible for all calculations related to vehicle dynamics such as sensor fusion of an accelerometer, gyroscope and GPS. It computes torque setpoints for each of the four independently controlled motors and transmits them periodically every 10 ms to converters. As a consequence, the speed loop was eliminated from the control algorithm, leaving only the conversion from requested torque to requested q current and the current control loop. Chapter 5 is dedicated to the current controller design process.

3.2 Voltage modulation

Electrical schematic of a three-phase, two level voltage source inverter (VSI) is shown in Figure 3.3. It is composed of six semiconductor switches organized in three pairs $S_{1,4}$, $S_{2,5}$ and $S_{3,6}$, one per phase. Each pair forms a structure known as a *half-bridge* or *phase leg* with one high side (HS) and low side (LS) switch (e.g. switches S1 and S4 in Figure 3.3, respectively). Phase legs function independently, each is connected to one terminal of the load. All phases are powered from the DC link – power delivering DC bus, typically connected to a battery or a rectifier – voltage U_{dc}. The star point of the load is labelled N, the DC link midpoint is labelled M. Although neither of them may be accessible for actual measurements, they are useful conceptually as levels of reference potential.

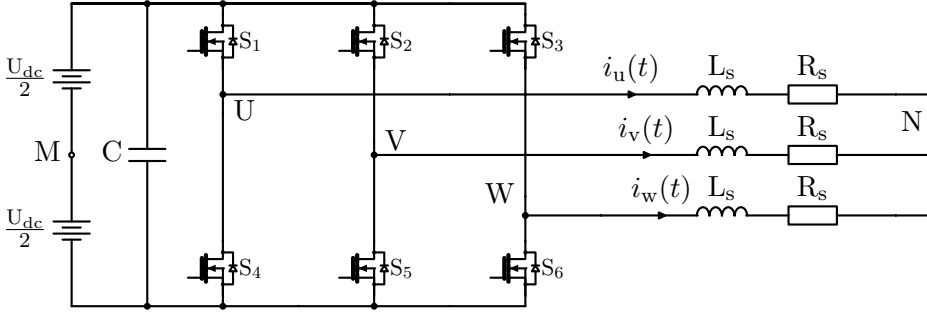Each pair of transistors is driven by a pair of complementary pulse width

Figure 3.3: Schematic of a three-phase VSI.

modulation (PWM) signals generated by an on-chip peripheral. Transistors do not switch off instantly and simultaneous activation of both high and low side switches – known as phase leg *shoot-through* – could have disastrous consequences for the inverter. This is prevented by inserting *dead time* – a delay between the deactivation of one switch and the activation of the other – into the driving waveform. The internal structure of power MOSFETs or details of their switching are outside of this thesis scope, however, they are covered in detail in [24]. Dynamics of MOSFETS are usually neglected for the modulator design due to their frequencies being higher by three or more orders of magnitude (more than 1000x).

To assess the overall effect of voltage applied on a given phase, the *volt-second* principle is introduced [3] – provided the switching frequency f_s is sufficiently high, the load does not experience individual short pulses of $u_\text{switched,M}$, but rather an average voltage

$$u_\text{phase,M} = \frac{1}{T} \int_{t_0}^{t_0+T} u_\text{switched,M}(t)\ \mathrm{d}t \tag{3.2}$$

observed over duration T, typically one switching period T_s. As there is only a finite set of discrete values of $u_\text{switched,M}$, the integral (3.2) simplifies to

$$u_\text{phase,M} = \frac{1}{T} \sum_k T_k u_\text{switched,M,}k, \tag{3.3}$$

a sum of applied voltages $u_\text{switched,M,}k$ weighed by durations of each application T_k. In a two-level inverter, each half-bridge is only capable of performing pulse width modulation (PWM) by connecting the phase to positive DC link rail for variable time T_1 and to the negative rail for $T_\text{s} - T_1$. Analyzing the voltage applied over a course of one switching period with assumption $u_\text{switched,M} = \pm U_\text{dc}/2$, equation (3.3) becomes [3]

$$
\begin{aligned}
u_\text{phase,M} &= \frac{1}{T_\text{s}} \left(T_1 \frac{U_\text{dc}}{2} + (T_\text{s} - T_1)\frac{-U_\text{dc}}{2} \right) \\
&= \frac{U_\text{dc}}{2T_\text{s}} (2T_1 - T_\text{s}) \\
&= \frac{U_\text{dc}}{2} \left(2\frac{T_1}{T_\text{s}} - 1 \right),
\end{aligned}
\tag{3.4}
$$

23

where the ratio T_1/T_s is the *duty cycle*[2], denoted DC. Therefore the voltage between each phase and the DC link midpoint M is an affine function of commanded duty cycle DC.

■ Modulation methods

The task of the modulator block is primarily to calculate the set of duty cycles for each transistor half-bridge, such that the voltages – now not referenced to the DC link midpoint, but rather to the star point N or even referenced to each other as line to line voltages – applied across machine terminals follow dq commands u_d, u_q requested by current regulators. Since there are many ways of achieving this – most of which are, however, only special cases of PWM – secondary objectives of modulation can be expressed through constraints. Comparison of individual modulation methods may utilize criteria such as the the maximal achievable line to line voltage, computation complexity, total harmonic distortion of current waveforms or the number of phase legs affected in every switching period.
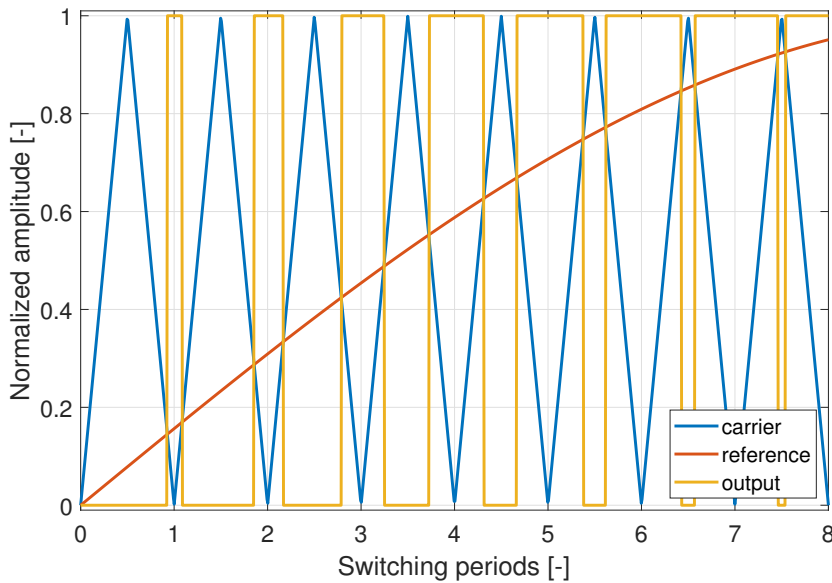
Figure 3.4: Detail of switching cycles of centre-aligned PWM.

Generation of PWM is illustrated in detail in Figure 3.4. The original message signal (shown in red) is compared with a high-frequency carrier shown in blue. The result of this comparison, shown in yellow, is directly the digital signal with DC dependent on the value of the message signal. In [3], an extensive analysis of the dependency of the current waveform frequency spectrum on the shape of the carrier is presented. This thesis only uses

---

[2]There are many competing definitions of the duty cycle, sometimes positive and negative duty cycles are distinguished etc. This definition is used in this thesis.

derived results about the superiority of centre-aligned PWM – i.e. triangular carrier waveform.
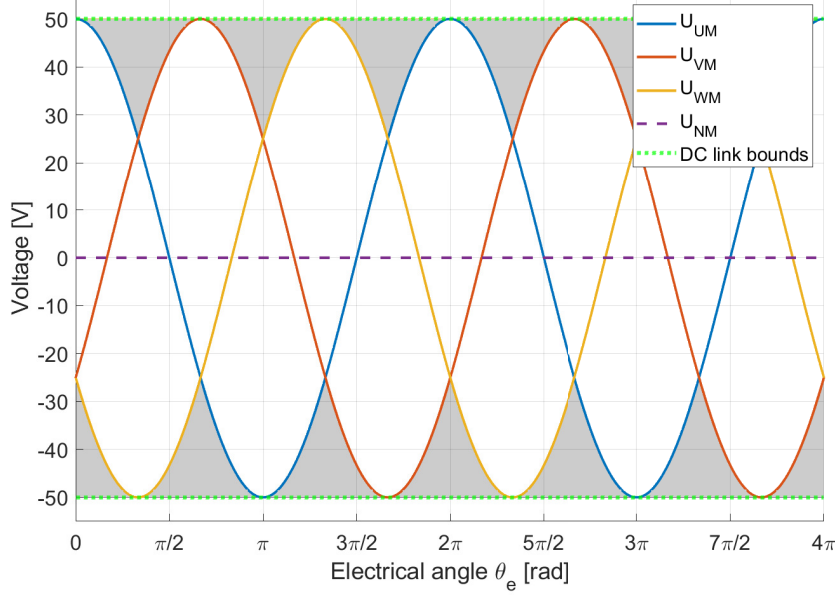
Figure 3.5: Phase voltages for sinusoidal modulation.

Sinusoidal modulation (SPWM) is the simplest modulation method used as a baseline. Requested voltages in *dq* reference frame undergo the inverse Park and Clarke transformations, resulting in reference waveforms for phase voltages, that are fed directly into the PWM module. An illustration of commands for individual phase legs is shown in Figure 3.5. The electrical displacement of phase voltages by 120° is observable, as well as the corresponding variance of duty cycles. For clarity, low carrier frequency is used, while in practice, there should be at least ten to twelve switching periods during one electrical revolution [3].

Since the connected load is not grounded anywhere, only line to line voltages are meaningful, rather than "absolute" phase voltages referenced to DC link midpoint. In Figure 3.5, sinusoidal phase voltages of greatest amplitude allowed by the DC link voltage U_{dc} are shown. There are, however, areas shaded in grey, representing available voltage that is not actively used to drive the machine. Therefore the greatest disadvantage of sinusoidal modulation is the fact, that it always utilizes at most

$$u_{\mathrm{l2l,max,SPWM}} = \frac{\sqrt{3}U_{\mathrm{dc}}}{2} \approx 0.866 U_{\mathrm{dc}}. \tag{3.5}$$

To simplify comparison of modulation methods, dimensionless quantity *modulation index M* is defined as

$$M = \frac{2u_{\mathrm{l2l}}}{\sqrt{3}U_{\mathrm{dc}}}, \tag{3.6}$$

25
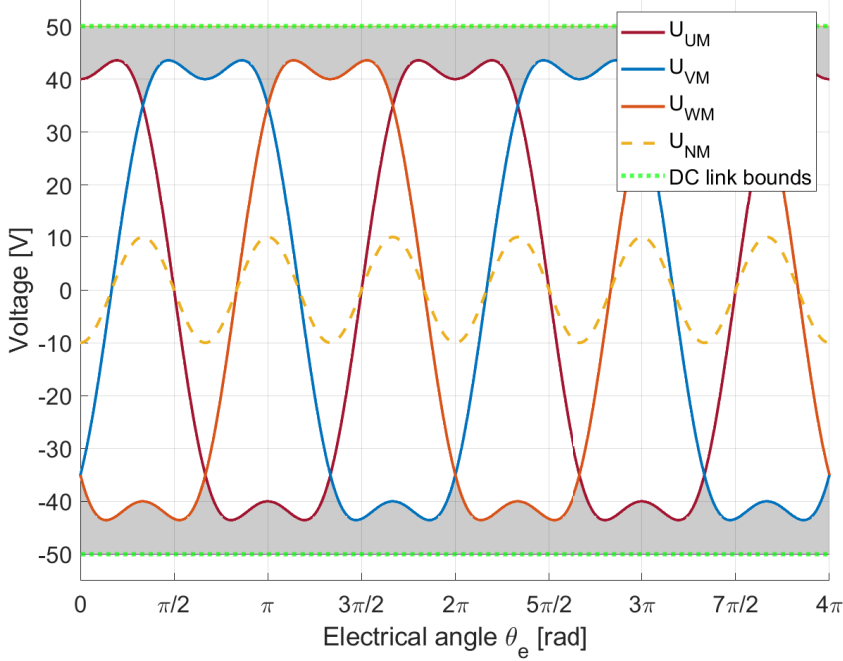
Figure 3.6: Phase voltages for sinusoidal modulation with injected third harmonic.

where u_{l2l} is the applied line to line voltage. From (3.5), the maximal modulation index of linear[3] sinusoidal modulation is $M = 1$.

Injecting a common mode third harmonic component u_{NM} into all phases offsets all phase waveforms such that the same line to line voltage can be applied across machine terminals, whilst decreasing the range of DC link voltages utilized, as can be seen in Figure 3.6. This method is called the *textitthird harmonic injection PWM* (THPWM). To fill the created grey band of unused potentials, the modulation index M can be increased to 1.15 without entering the region of overmodulation. The optimal amplitude of said common-mode component is one sixth of the amplitude of the fundamental component [3]. The same modulation index can be achieved with the more widely spread *space vector modulation* (SVM), principles of which are summarized in [25] or [4]. SVM has been heavily optimized for digital calculations, as shown e.g. in [26]. THPWM on the other hand offers simpler insight into the principle of operation and is not significantly more expensive to calculate due to the availability of the CORDIC coprocessor.

The common-mode component is calculated as follows. The requested dq voltages $\vec{u}_{dq}$ and the instantaneous electrical angle θ_e enter the modulator. Like in the case of sinusoidal modulation, the inverse Park and Clarke transformations are calculated to obtain phase voltages $\widetilde{\vec{u}_{uvw}}$. Then, the

---

[3]without entering the overmodulation region

26
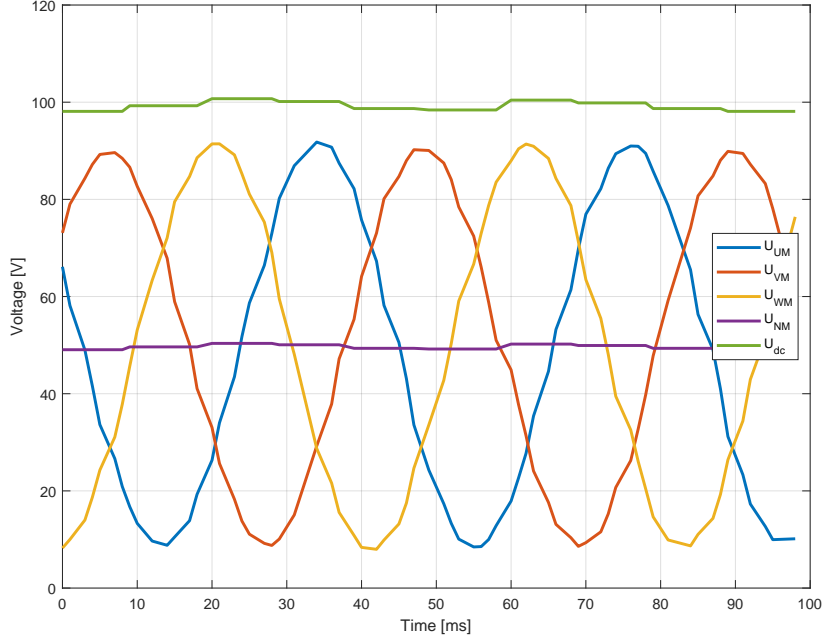
Figure 3.7: Waveforms generated by normal sinusoidal modulation.

common-mode component is calculated using

$$u_{\mathrm{NM}} = -\frac{U_{\mathrm{dc}}}{6\sqrt{3}} \cos 3\left(\theta_{\mathrm{e}} + \operatorname{atan2}(u_{\mathrm{q}},\, u_{\mathrm{d}})\right), \tag{3.7}$$

where the scaling coefficient is independent of the currently requested amplitude of phase voltages to simplify calculation. It considers the most pessimistic case, i.e. when the line to line voltage is equal to the full DC link range, division by $\sqrt{3}$ converts line to line voltage to line to neutral voltage, which is divided by six to find the amplitude of the common mode component. Finally, phase voltages

$$\vec{u}_{\mathrm{uvw}} = \widetilde{\vec{u}_{\mathrm{uvw}}} + u_{\mathrm{NM}} \tag{3.8}$$

are fed into the PWM module.

To assess functionality of the implementation, generated phase voltages have been transmitted from the microcontroller to the master computer and visualized. Due to tooling limitations, data was acquired at sampling frequency only 400 Hz causing some additional distortion of waveforms. Waveforms were recorded at speed constant $n \approx 900 \,\mathrm{RPM}$ and current $I_{\mathrm{q}} = 10 \,\mathrm{A}$. Waveforms generated by the sinusoidal modulation are shown in Figure 3.7.

In Figure 3.8, phase voltages generated by injecting the third harmonic are displayed. Although real waveforms are not as smooth as simulation results in Figure 3.6, line to line voltages plotted in Figure 3.9 are sinusoidal.

Figure 3.8: Phase voltages for THPWM.
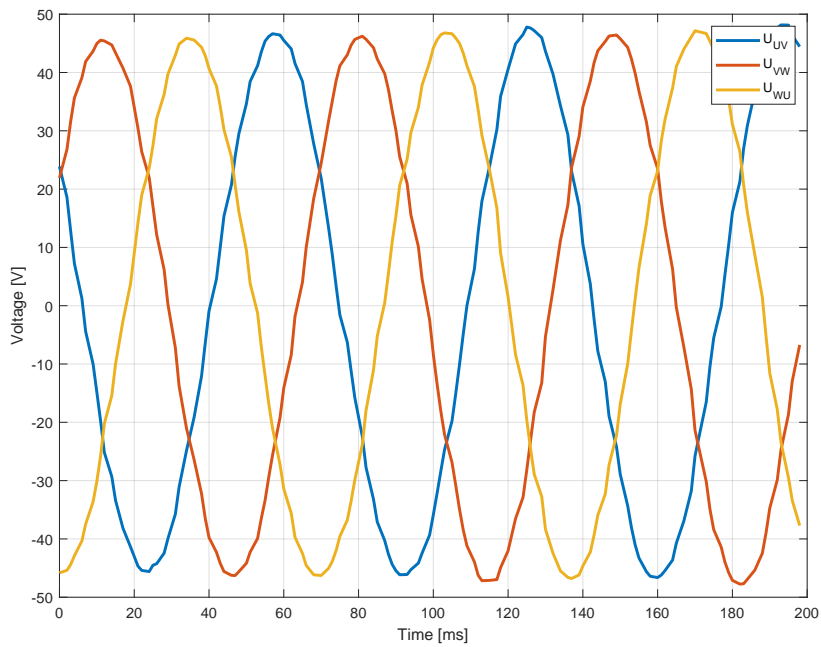
Figure 3.9: Line to line voltages for THPWM.

Chapter 4

Rotor angular position measurement

Knowledge of the precise angular position of the motor's rotor is an essential piece of information used for FOC. It is crucial for forward Park transformation to calculate the current vector in *dq* reference frame and later for voltage modulation. Due to requirements on the accuracy of shaft angle information specific to PMSM control,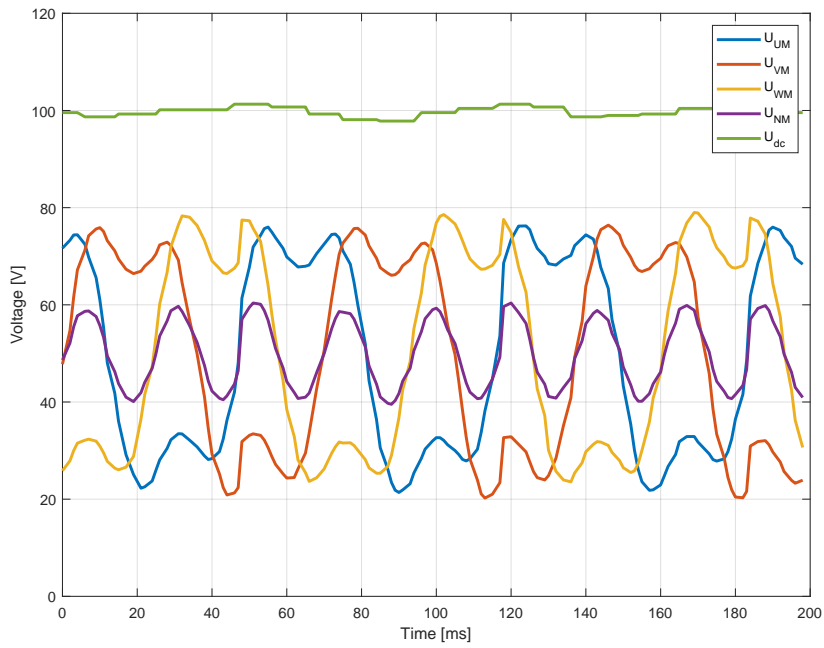 low-resolution angular position sensors, such as Hall effect transducers, are insufficient. Two predominantly used types of sensors in the PMSM motor control environment are encoders and resolvers. Alternatively, sensorless methods do not need any sensor in the first place. This section discusses various methods of angular position calculation with emphasis on the resolver since it is the sensor of choice in motors of electric vehicles designed by eForce.

4.1 Sensorless approach

A lot of research effort has been aimed at the so-called *sensorless control* – the possibility to apply one of vector control strategies to a motor without direct feedback from a shaft angle sensor, reducing the manufacturing cost and increasing reliability. An observer of the motor model is devised, estimating the motor states based on known values of action signals and measurable system outputs, i.e. phase currents. The complexity of said observer varies greatly, even using artificial intelligence through trained neural networks, such as in [27]. In general, model-based sensorless strategies tend to perform better at higher speeds and fall behind at low speed operation due to the decreased magnitude of BEMF voltage [28].

To illustrate at least one of the many principles, a family of methods for sensorless shaft angle estimation is based around motor saliency (2.22) different from unity. A high frequency voltage $\vec{u}_{\alpha\beta}$ – 500 Hz when idle but up to 2.5 kHz during operation, so as not to interfere with lower-frequency signal controlling the motor's torque – is injected into the motor, whose current response $\vec{i}_{\alpha\beta}$ is analyzed. Assuming a linear electrical system, both vectors

are related through the impedance **Z**, written in the matrix form as

$$\begin{bmatrix} u_\alpha \\ u_\beta \end{bmatrix} = \underbrace{\begin{bmatrix} Z_{\alpha\alpha}(\theta_e) & Z_{\beta\alpha}(\theta_e) \\ Z_{\alpha\beta}(\theta_e) & Z_{\beta\beta}(\theta_e) \end{bmatrix}}_{\mathbf{Z}} \begin{bmatrix} i_\alpha \\ i_\beta \end{bmatrix}. \tag{4.1}$$

Provided the injected frequency is high enough, resistive components of the impedance matrix are dominated by the magnitude of reactance $j\omega_e L_{d,q}$ and are neglected. Assuming that $L_{d,q}$ are known, individual elements of the complex impedance matrix **Z** in (4.1) are non-linear functions of a single variable θ_e, allowing its extraction [28].

Sensorless motor control is – in comparison with sensored control described in the rest of this thesis – more advanced and is outside of this thesis scope. Overview of other successful strategies can be found in [29], [30], while an elaborate presentation is given e.g. in [31].

4.2 Encoder feedback

The simplest encoder, suitable e.g. for knobs in consumer electronics, is an *incremental encoder* with a *quadrature output* signal shown in Figure 4.1. In its essence, the incremental encoder is composed of two parts – a rotating disc mounted e.g. on the motor shaft and a pair of stationary sensing heads A and B spaced an odd multiple of $\Delta\theta/2$, where $\Delta\theta$ is the angular resolution, apart. The rotating disc is composed of discrete alternating sectors (such as magnetic poles or conductive planes connected to high or low voltage to name a few) depending on the underlying physical principle. Each sensing head produces either a high or low output level based on the instantaneous properties of sector beneath it. In Figure 4.2, an optical encoder is illustrated, for which either of the output signals is high when the photodetector senses light from the LED.
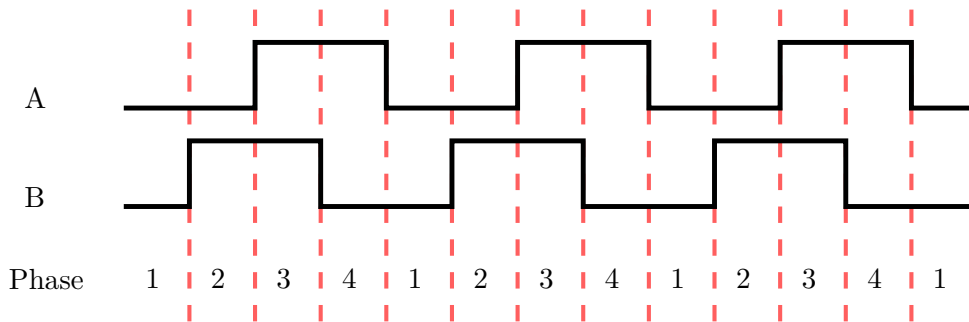

Figure 4.1: Timing diagram of quadrature encoder signal, from [32]

As the disc rotates, the edge on either A or B output indicates a transition of the corresponding sensing head from one sector to another. Due to spacing, one head observes a transition sooner than the other, phase shifting edges on A and B signals by 90° in the steady-state and producing anywhere from 2^9
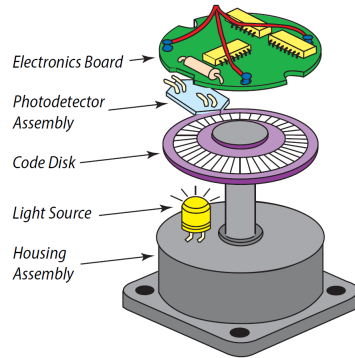
Figure 4.2: Example of the structure of an optical encoder, taken from [33].

to 2^{16} *counts per revolution* (CPR) for a typical industrial encoder. Various practical aspects of encoder feedback are discussed in [34], such as that for high speed applications, the accuracy is usually decreased due to accumulated time delay in the system.

All encoder signals are digital, significantly improving the resistance to noise, which may be further increased by following the manufacturer's recommendations such as [35]. Due to high resolution and accuracy, the encoder is sensitive even to small movement, making it suitable for precise applications [36]. On the other hand, the incremental encoder produces information about speed and direction only, leaving the initial angle unknown. Absolute angle encoders are created by essentially multiplying the described basic structure, placing n sensing heads and rotating discs, each having an increasing power of two sectors, next to each other. Now using only one of the outputs from each level, n digital signals are acquired, creating a n-bit binary number representing the absolute angular position.

4.3 Resolver feedback

The resolver is an analog sensor of absolute angular position with history going back to World War II. It is essentially a rotating transformer with one primary winding and two electrically orthogonal secondary windings. When a sinusoidal signal

$$u_{\mathrm{exc}}(t) = U_{\mathrm{exc}} \sin(2\pi f_{\mathrm{exc}} t) \tag{4.2}$$

with amplitude U_{exc} and frequency f_{exc} is applied to the primary excitation winding, the magnetic field is transferred through the rotating core mechanically mounted on the rotor to both secondary windings, inducing sinusoidal voltages. This structure is illustrated in Figure 4.3. An overview of alternative mechanical structures is presented in [37].

As the rotor spins, coefficients of coupling and hence mutual inductances to both secondary windings change, resulting in an amplitude modulation of sine and cosine of the instantaneous rotor angle θ_{r} onto the carrier $u_{\mathrm{exc}}(t)$. This property is reflected by nomenclature, using labels SIN and COS for
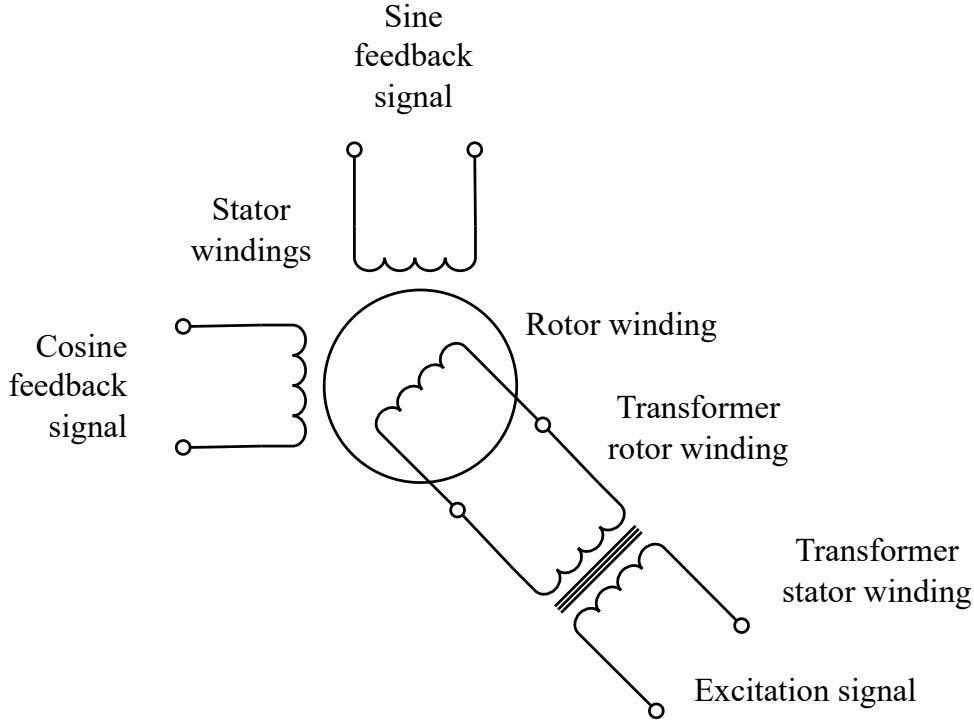
Figure 4.3: Internal structure of a brushless resolver, from [11], Figure A5.3.

said secondary windings. Provided[1] $\omega_r = \dot{\theta}_r \ll 2\pi f_{\text{exc}}$, signals induced on secondary windings are

$$
\begin{aligned}
u_{\sin}(t) &= u_{\text{exc}}(t)T_r \sin\theta_r, \\
u_{\cos}(t) &= u_{\text{exc}}(t)T_r \cos\theta_r
\end{aligned}
\tag{4.3}
$$

for SIN and COS secondary winding, respectively. Parameter T_r is the resolver transformation ratio and θ_r is the measured resolver angle. An illustration of output waveforms (4.3) is shown in Figure 4.4. Envelopes of sine and cosine signals are highlighted by black dashed lines. One of them, denoted by a thicker dashed line, is exactly the message signal of interest, i.e. the sine and cosine of resolver angle θ_r.

The mechanical angle of the rotor

$$
\theta_m = \frac{1}{n_r}\left(\theta_r - \theta_{\text{off}}\right)
\tag{4.4}
$$

is an affine function of the resolver angle θ_r, where $n_r \in \mathbb{N}$, $n_r \geq 1$ is the number of resolver pole pairs[2] and θ_{off} is an optional constant offset. Its importance lies in the conversion from θ_r to the electrical angle θe, since resolver zero[3] is in reality not necessarily aligned with the direction of phase

---

[1]This is indeed fulfilled in the current design with $f_{\text{exc}} = 10\,\text{kHz}$ and maximal frequency of mechanical rotation approximatelly $330\,\text{Hz}$ (see Section 1.2).

[2]Multiple resolver pole pairs may be used, increasing the angular resolution. The underlying principle is essentially the same as for multi-pole-pair motors, see Section 2.2.4.

[3]i.e. the specific angle for which $u_{\sin}(t)$ is zero and $u_{\cos}(t)$ is at maximal amplitude.
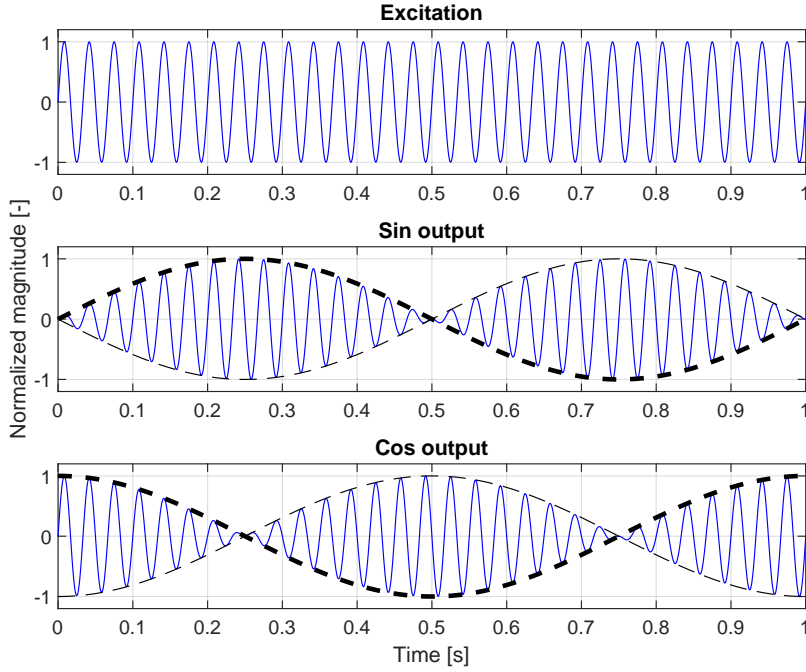
Figure 4.4: Resolver signal waveforms

U, defined as $\theta_e = 0$. Therefore, by combining (4.4) with (2.19), the relation

$$\theta_e = \frac{n_p}{n_r} \left(\theta_r - \theta_{off} \right) \tag{4.5}$$

of resolver angle θ_r and the electrical angle θ_e is found.

The resolver has many beneficial properties, making it suitable for hostile environments [38], [39] – it is mechanically very robust and the magnetic principle of operation makes it appropriate for industrial environment, where omnipresent dirt and grease render fragile optical encoders unusable. Furthermore, all windings are electrically insulated from each other and both excitation, as well as sine and cosine outputs, are transmitted as differential signals, significantly reducing susceptibility to common-mode noise.

The extraction of immediate rotor angle θ_r from SIN/COS signals as well as the AM demodulation itself could be implemented in several ways. There are various methods of analog envelope extraction for amplitude demodulation, ranging from passive circuits consisting of a diode and RC filter to active peak detectors, such as the one proposed in [38]. Specialized integrated circuits, commonly known as *resolver converters*, are designed to directly interface with the resolver and output either digital or analog signals proportional to shaft angle and angular frequency. The design of such an integrated circuit is presented in detail in [39].

However, envelope extraction in the digital domain is favourable due to reduced hardware cost and complexity. As discussed in the following section, state estimators are typically connected to the resolver output. The ease

of tuning of a digital system and its time- and temperature invariance are beyond comparison with an analog circuit. Implementation of this thesis employed the synchronous demodulation described in [40], when a new sample is taken every half-period of excitation, exactly at its maximum or minimum.

A note should be made in passing regarding the two main resolver errors. According to [40], they are

- the *amplitude error* caused by a difference in transformation ratio from excitation to either secondary winding, and

- the *quadrature error*, when the envelope of sine is not lagging exactly 90° behind cosine.

A detailed analysis is performed in [41], followed by a proposition of a simple correction mechanism, parameters of which, however, are not easy to identify. The practical implementation was rather concerned with simpler errors, such as a non-zero DC offset of both resolver outputs after conditioning by analog front-end. Intricate details of errors of the resolver itself were therefore not investigated further.

4.4   Angle tracking observer

While it is theoretically possible to extract the immediate rotor angle from resolver signals using the inverse tangent function[4], the practical usefulness of this approach is severely reduced. First of all, the evaluation of the inverse tangent is normally[5] computationally very expensive, consuming valuable processing cycles of digital logic running the motor control algorithm.

Second of all, there is the inherent property of all analog signals – noise susceptibility. Since the information about speed is valuable for the control algorithm, a numerical differentiation would have to be implemented, amplifying the noise even further. Although some improvement could be achieved using a noise suppression filter, it would only increase the phase lag, possibly threatening system stability.

The state-of-the-art solution for obtaining noise-free estimates of angular position $\hat{\theta}_\mathrm{r}$ and speed $\hat{\omega}_\mathrm{r}$ is the angle tracking observer (ATO). It is a closed-loop dynamic system connected to resolver output. The estimated angle is subtracted from the resolver output to yield an observation error $e = \theta_\mathrm{r} - \hat{\theta}_\mathrm{r}$. This error is fed into a regulator with transfer function $C(s)$, whose output $\hat{\omega}_\mathrm{r}$ is then integrated to acquire angle estimate $\hat{\theta}_\mathrm{r}$. One of possible structures is displayed in Figure 4.5.

Although the hardware implementation of ATO using multiplying digital to analog converters and a phase-locked loop is possible, as shown in [11], it is nowadays rather rare due to non-ideal properties of operational amplifiers and other hardware components. Moreover, digital implementation is far superior due to the ease of loop tuning and temperature and time invariance.

---

[4]Especially – from the implementation point of view – its four-quadrant version `atan2(y,x)`

[5]without the utilization of the CORDIC coprocessor
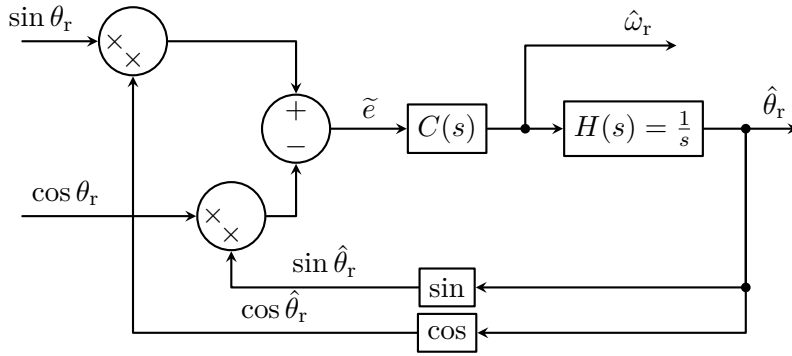
Figure 4.5: Angle tracking observer structure.

■ 4.4.1 Observation error

Observation error fed into the controller $C(s)$ should ideally be $e = \theta_r - \hat{\theta}_r$, however the precise angle θ_r is not known – if it were, no observer would be needed in the first place. There are two options:

1. Calculate $\theta_r = \mathrm{atan2}(\sin\theta_r, \cos\theta_r)$ and subtract the estimated $\hat{\theta}_r$.
   This is typically the inferior alternative due to disadvantages connected with the evaluation of inverse tangent discussed in Section 4.4. Since modern microcontrollers contain the CORDIC coprocessor allowing extremely fast calculation of inverse tangent, this method will be assessed as well.

2. Calculate $\sin\hat{\theta}_r$, $\cos\hat{\theta}_r$ and approximate the true error.
   Sine and cosine are significantly cheaper to evaluate, typically using either lookup tables or several terms of Taylor series expansion. Using the CORDIC coprocessor, both sine and cosine can be calculated rapidly and in parallel. This implementation is also feasible by purely hardware implementation.

The calculation of observation error based on a trigonometric identity uses the small angle approximation

$$\sin x \approx x, \quad \text{when } x \text{ is small,} \tag{4.6}$$

and the difference of angles identity for sine

$$\sin(x - y) = \sin x \cos y - \cos x \sin y. \tag{4.7}$$

Putting (4.6) and (4.7) together yields the regulator input

$$\widetilde{e} = \sin\theta_r \cos\hat{\theta}_r - \cos\theta_r \sin\hat{\theta}_r = \sin(\theta_r - \hat{\theta}_r) \approx \theta_r - \hat{\theta}_r = e, \tag{4.8}$$

that is actually no longer precisely equal to the observation error e, but is a sufficient approximation under conditions discussed below. Several real world considerations must be addressed when implementing the equation (4.8).

◼ Angle periodicity

First, the system must correctly handle the periodicity of angle representations. From the motor control algorithm's point of view, only the angle normalized to range $[-\pi, \pi)$ is relevant. For this reason alone, utilization of fixed point representation is very natural, as the two's complement arithmetic inherently takes care of wraparound[6] of both angle estimate $\hat{\theta}_\mathrm{r}$ as well as observation error e. This aspect will be explored further in Section 4.4.3.

◼ Correctness of small angle approximation

The second consideration is the importance of the small angle requirement imposed by the use of (4.6). The relative error between sine and a linear approximation exceeds 1% around 0.25 rad, which is more than enough for the steady-state when the value of observation error $e \approx 0$ is expected. Figure 4.6 shows two curves - the real estimation error and the apparent error calculated using the approximation (4.8). Note the previously discussed periodicity of both functions.

It can be argued that even for $||e|| \gg 0$, the error calculation will yield reasonable results. Although sine is not strictly increasing and hence greater estimation error e does not necessarily cause a greater regulator input $\widetilde{e}$, at least

$$\operatorname{sign} e = \operatorname{sign} \widetilde{e}. \tag{4.9}$$

Therefore – if the observer is correctly designed – the system will be stable and the observation error will tend to zero for arbitrary non-zero initial condition e_0. The only exception is an initial observation error $e_0 = \pi$, for which $\widetilde{e}_0 = 0$ and the observer is in an unstable equilibrium. Even the small measurement noise is a sufficient disturbance, making the observer leave the unstable equilibrium and eventually settle in the stable equilibrium with $e_\mathrm{ss} = \widetilde{e}_\mathrm{ss} = 0$.

◼ Multiplicative error on both outputs

The third possible problem is caused by a simultaneous multiplicative error on both demodulated signals $\sin \theta_\mathrm{r}$ and $\cos \theta_\mathrm{r}$. Assume for a moment that the resolver coupling coefficient suddenly decreases by a factor of $\alpha < 1$. From (4.3), both SIN and COS outputs will decrease by α as well, and the regulator input in (4.8) becomes

$$(\alpha \sin \theta_\mathrm{r}) \cos \hat{\theta}_\mathrm{r} - (\alpha \cos \theta_\mathrm{r}) \sin \hat{\theta}_\mathrm{r} = \alpha \sin(\theta_\mathrm{r} - \hat{\theta}_\mathrm{r}) = \alpha \widetilde{e}. \tag{4.10}$$

The resolver transformation ratio is unlikely to significantly change under normal circumstances, except for possible electromechanical failures such as damaged wiring or free play in the mechanical assembly. What may change,

---

[6]Integer overflow and underflow in mod 2^N arithmetic bring large positive and negative values closer together, which corresponds to the negligible difference between angles π and $-\pi$ radians.
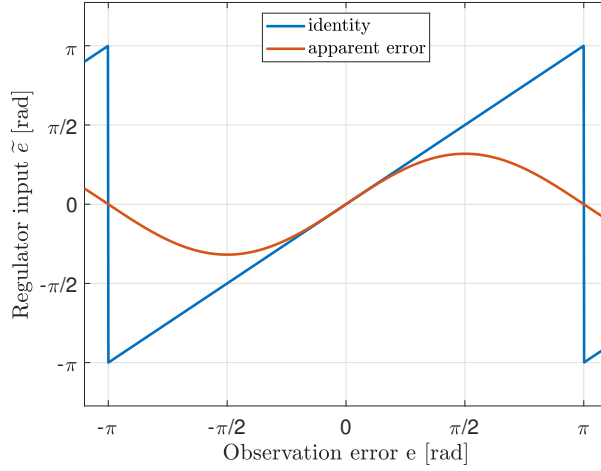
Figure 4.6: Regulator input $\widetilde{e}$ as a function of estimation error e.

however, are the transfer functions of other used components – both excitation filters as well as ADC anti-aliasing filters – e.g. due to the temperature dependence of component parameters. As a result, the relative phase of resolver outputs and ADC triggering system may change slightly, such that signals are no longer sampled in their local extrema. This inherently decreases the apparent amplitude of both SIN/COS signals, hence – from (4.10) – decreasing the magnitude of regulator input $\widetilde{e}$ in the process. This slows down the observer but otherwise causes no problems for stability. This phenomenon is discussed in [40] with the same conclusion.

4.4.2 Observer design

In the steady-state, the motor angular speed ω_r is constant and the angle θ_r grows linearly. It immediately follows that the open-loop ATO transfer function shall be of type[7] no less than 2, so that the estimate $\hat{\theta}_\mathrm{r}$ can track a ramp reference $\theta_\mathrm{r}(s) = 1/s^2$ with zero steady state error. One integrator is already present in $H(s)$ (conversion from $\hat{\omega}_\mathrm{r}$ to $\hat{\theta}_\mathrm{r}$), therefore the other one must be present in the regulator $C(s)$.

The observed system may be modelled in a state-space form

$$\frac{\mathrm{d}}{\mathrm{d}t}\theta_\mathrm{r} = \omega_\mathrm{r},$$
$$\frac{\mathrm{d}}{\mathrm{d}t}\omega_\mathrm{r} = f(\ldots),$$
(4.11a)

$$y = \theta_\mathrm{r},$$
(4.11b)

with output equation (4.11b), where $f(\ldots)$ represents unknown system dynamics. In [44], a generic velocity observer of order m is proposed, considering

---

[7]The *type* of a system is defined as the natural number N denoting the number of poles in the s-plane origin, i.e. the character of system's integral response. A type-N system is capable of tracking a $(N-1)$-th degree polynomial like reference. See [42], [43].

$m - 1$ derivatives of estimated angular position $\hat{\theta}_{\mathrm{r}}$ and achieving a stable transfer function from unknown dynamics and measurement noise to the estimated angular frequency $\hat{\omega}_{\mathrm{r}}$. It is shown that lower-order observers have better noise-rejection properties and comparable tracking performance for fast (roughly more than $2\,\mathrm{Hz}$) dynamics of $f(\ldots)$. On the other hand, during operation closer to steady-state in the low-frequency range, higher-order observers manifested better performance and smoother tracking. Similarly, assessing estimators of a different order but equal bandwidth, the faster the observer, the stronger the noise amplification.

Based on the presented results, a second-order observer has been chosen as a baseline. Considering the transfer function of a generic PI controller $C(s)$, connected in series with the integrator $H(s)$, the open-loop transfer function is

$$OL(s) = C(s)H(s) = \frac{K_p s + K_i}{s} \cdot \frac{1}{s}. \tag{4.12}$$

Closing the loop yields the transfer function

$$ATO(s) = \frac{OL(s)}{1 + OL(s)} = \frac{K_p s + K_i}{s^2 + K_p s + Ki}, \tag{4.13}$$

whose denominator may be compared to a general second-order system

$$G(s) = \frac{\omega_{\mathrm{n}}^2}{s^2 + 2\omega_{\mathrm{n}}\zeta s + \omega_{\mathrm{n}}^2} \tag{4.14}$$

with natural frequency ω_{n} and damping coefficient ζ to acquire regulator constants

$$\begin{aligned} K_p &= 2\zeta\omega_{\mathrm{n}}, \\ K_i &= \omega_{\mathrm{n}}^2 \end{aligned} \tag{4.15}$$

as functions of the desired system dynamics. The closed loop has a stable[8] zero at $-\frac{K_i}{K_p}$, cancellation of which may be considered later.

The desired closed-loop ATO dynamics are dictated by unknown dynamics $f(\ldots)$, mostly stemming from the mechanical domain. Based on the discussion in Section 2.2.3 and results presented in [44], the observer is chosen rather slow with natural frequency $70\,\mathrm{rad\,s^{-1}}$.

Other improvements to the observer structure shown in Figure 4.5 have been proposed in the literature. For example, a third-order observer based on the Chebyshev filter approximation is proposed in [45], achieving even smoother $\hat{\omega}_{\mathrm{r}}$ at the expense of slightly worse angle tracking. However, it is shown that the estimated angle is already sufficiently free of noise and therefore a less noisy $\hat{\omega}_{\mathrm{r}}$ could be valuable for feedforward compensation designed later in (5.3).

■ 4.4.3 Digital implementation

For reasons discussed in Section 4.4.1 and since the CORDIC coprocessor interface only accepts signed numbers in `Q1.15` or `Q1.31` fixed point format –

---

[8]$K_p, K_i > 0$ follows directly from (4.15) and reasonable choice values of ω_{n} and ζ.

properties of which are compared in Table 4.1 – the ATO was implemented using fixed point arithmetic. In contrast with floating point numbers, there is no need for specialized fixed point instructions. Normal integer arithmetic instructions can be used for fixed point calculations, making it especially lucrative for real-time digital signal processing in FPGAs or DSPs.

■ Fixed point number representation

A fixed point number of word length n with m^9 fractional bits is internally nothing more than a plain n-bit integer i. It is assigned special meaning by the designer using e.g. the *per unit* (PU) system discussed in [46]. For a given scaling constant A (typically a nominal value of the quantity in question), the actual physical value p represented by the fixed point number is

$$p = A\frac{i}{2^m},\tag{4.16}$$

where i is called the *stored integer* of quantity p, denoted p^{i} to reduce verbosity in the text below. For example, the stored integer $u^{\mathrm{i}} = -4000$ using PU model `Q1.15` with maximal value $A = U_{\max} = 100\,\mathrm{V}$ represents voltage

$$u = 100 \cdot \frac{-4000}{2^{15}} = -12.2\,\mathrm{V}.$$

The overall usefulness of the per unit system in the motor control environment, especially as a natural means of comparison of different machines with largely different rated parameters, is discussed further in [4], [10], [31].

Unless explicitly indicated otherwise, physical value is meant when talking about a fixed point number. Arbitrary combinations of n, m and A are possible and used in FPGA designs, however, for designs based around a general-purpose digital computer, n is typically chosen to be a power of two. Furthermore, choosing $m = n - 1$ yields representable range $2^{-m}p^{\mathrm{i}} \in [-1, 1)$, therefore $p \in [-A, A)$. The scaling coefficient A then coincides with the maximal expected value, possibly plus some margin for safety. A fixed point representation with an equal number of bits as a given floating point number has comparably lower dynamic range but constant quantization step and greater resolution across the whole value range (as is apparent from Table 4.1), making it more resilient to rounding errors during long multiply-accumulate operations.

The CORDIC coprocessor interface dictates choice of $A = \pi$, such that all angles φ are represented in radians and normalized by π, i.e. $2^{-m}\varphi^{\mathrm{i}} \in [-1, 1)$ corresponds to physical values $\varphi \in [-\pi, \pi)$. Incrementing φ^{i} past 2^m (representation of $\varphi = \pi$) overflows and gives some value close to -2^m, naturally handling the periodicity.

---

[9]Condition $m < n$ is self-evident. Possibly $m = n$ for unsigned fixed point data types.

Data type	Q1.15	Q1.31	IEEE754 `float`[10]
Word length [bits]	16	32	32
Fractional bits	15	31	23
Dynamic range	$6.554 \cdot 10^4$	$4.295 \cdot 10^9$	$3.403 \cdot 10^{76}$
Resolution	$3.052 \cdot 10^{-5}$	$4.657 \cdot 10^{-10}$	not constant

Table 4.1: Comparison of fixed point and floating point data types.

◾ Regulator discretization

Using the *forward difference* discretization method, continuous-time dynamic blocks in Figure 4.5 were discretized as

$$H(z) = \frac{T_s}{z - 1}, \tag{4.17a}$$

$$C(z) = K_p + \frac{T_s K_i}{z - 1}, \tag{4.17b}$$

where $T_s = f_s^{-1}$ is the sampling period. Manipulating (4.17a) and applying the inverse $\mathcal{Z}$-transform yields the difference equation

$$\hat{\theta}_{\mathrm{r}}(n) = T_s \hat{\omega}_{\mathrm{r}}(n - 1) + \hat{\theta}_{\mathrm{r}}(n - 1), \tag{4.18}$$

not yet in the most optimal form for software implementation.

Due to the linearity of all involved systems, signals may be scaled by a constant without affecting the result, as long as an inverse gain is applied later. Whereas the representation of angles is dictated by the CORDIC coprocessor interface, scaling of $\hat{\omega}_{\mathrm{r}}$ can be chosen. A simple optimization would be to scale $\hat{\omega}_{\mathrm{r}}^{\mathrm{i}}$ additionally by $1/T_s = f_s$, cancelling the multiplication in (4.18) and converting it to

$$\hat{\theta}_{\mathrm{r}}^{\mathrm{i}}(n) = \hat{\omega}_{\mathrm{r}}^{\mathrm{i}}(n - 1) + \hat{\theta}_{\mathrm{r}}^{\mathrm{i}}(n - 1), \tag{4.19}$$

appropriate for direct implementation in software.

It is clear that after multiplication by $f_s = 2 \cdot 10^4$, the dynamic range of `Q1.15` would not suffice anymore, causing large quantization errors at low speeds. To simplify the implementation, all values (estimated states as well as regulator constants) were converted to the same data type `Q1.31`. In summary, ATO quantities are represented as

$$\begin{aligned}
\hat{\theta}_{\mathrm{r}} &= 2^{-31} \pi \hat{\theta}_{\mathrm{r}}^{\mathrm{i}} \ [\mathrm{rad}], \\
\hat{\omega}_{\mathrm{r}} &= 2^{-31} f_s \pi \hat{\omega}_{\mathrm{r}}^{\mathrm{i}} \ [\mathrm{rad\,s^{-1}}], \\
\widetilde{e} &= 2^{-31} \widetilde{e}^{\,\mathrm{i}} \ [\text{-}],
\end{aligned} \tag{4.20}$$

which has to be taken into consideration when programming regulator gains.

Inverse $\mathcal{Z}$-transform and subsequent manipulations applied on (4.17b) yield

$$\hat{\omega}_{\mathrm{r}}(n) = \hat{\omega}_{\mathrm{r}}(n - 1) + K_i T_s \widetilde{e}(n - 1) + K_p(\widetilde{e}(n) - \widetilde{e}(n - 1)). \tag{4.21}$$

Plugging (4.20) into (4.21) gives a simple difference equation in terms of stored integers

$$\hat{\omega}_{\mathrm{r}}^{\mathrm{i}}(n) = \hat{\omega}_{\mathrm{r}}^{\mathrm{i}}(n-1) + \underbrace{\frac{K_i}{f_s^2 \pi}}_{\widetilde{K_i}} \tilde{e}^{\mathrm{i}}(n-1) + \underbrace{\frac{K_p}{f_s \pi}}_{\widetilde{K_p}} (\tilde{e}^{\mathrm{i}}(n) - \tilde{e}^{\mathrm{i}}(n-1)), \qquad (4.22)$$

appropriate for real-time software implementation. Calculation of new regulator gains $\widetilde{K_p}$ and $\widetilde{K_i}$ is left on the C++ compiler, allowing the engineer to input desired continuous-time gains (4.15) without bothering with manual discretization, whilst guaranteeing no runtime performance degradation.

Since the software has access to the closed-form expressions for discrete-time controller gains, on thy fly recalculation is possible, enabling a variable sample rate architecture. Its benefits include lower power consumption e.g. when the controlled system is idle, as discussed in [47] and [48]. Follow-up work should investigate the implementation of variable sample rate, striking balance between low power consumption and high dynamic performance when needed.

4.5 Performance evaluation

Both methods of obtaining the observation error discussed in Section 4.4.1 were implemented in the motor controller firmware. The first one, based on evaluation of `atan2`, is abbreviated as "CORDIC" to emphasize dependence on the trigonometric coprocessor. The second one, using a trigonometric identity, is abbreviated "TRIGIDEN".

The usefulness of an ATO is proven in Figure 4.7, where the estimated angle $\hat{\theta}$r is compared to the unfiltered raw resolver reading. Even with equal controller gains, the dynamics of both observer architectures differ. A comparison of magnitudes of the observation error shown in Figure 4.8 is a manifestation of the difference of gain in both closed loops. Therefore, from (4.10), the TRIGIDEN architecture requires a slightly greater observation error for the same response in comparison to CORDIC architecture.

The lower gain in the TRIGIDEN closed-loop manifests itself by a smaller overshoot of the ATO step response. As shown in Figure 4.9, where a step-like disturbance was simulated by resetting the microcontroller power supply, the more aggressive CORDIC is slightly less damped and therefore takes longer to settle in the steady-state. Such an input stimulus is, however, not practically relevant, as the angular position always changes continuously and relatively slowly, never exposing the observer to a step-like input during normal operation. Correction of this deficiency is possible by identifying the resolver gain and inverting it in firmware, effectively normalizing both sin and cos signals.
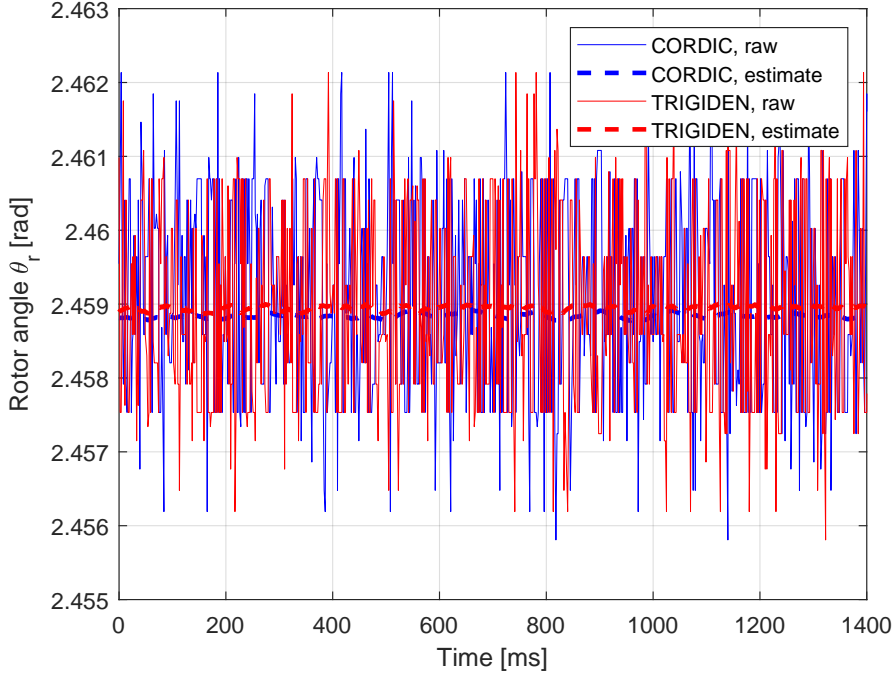
Figure 4.7: Angle tracking observer noise rejection.

4.6 Transport delay analysis

There are at least two zero-order holds in the system – sampling by the ADC and the PWM module – each adding a time delay of at least half a sampling period long. In [49], combined delay of all digital blocks is estimated to be

$$T_{\mathrm{delay}} = 1.5\,T_{\mathrm{s}},$$

where T_{s} is the sampling interval, equating to $75\,\mu\mathrm{s}$ for the chosen sampling frequency $f_{\mathrm{s}} = 20\,\mathrm{kHz}$. Other effects of the transport delay are analyzed in [50], concluding that current loop instability may occur. A solution utilizing the Smith predictor is proposed in [51], achieving good results even in the case of very long sensor transport delays up to $5\,\mathrm{ms}$. Since the motor itself is assumed not to have a significant transport delay in the electrical domain and its electrical time constant is in the order of milliseconds, all transport delays are neglected in the design of the current loop regulation discussed in Section 5.

Where the time delay certainly can't be neglected, is the shaft angle estimation. With a maximal mechanical frequency $f_{\mathrm{m}} = 333\,\mathrm{Hz}$ and $n_{\mathrm{p}} = 4$ pole pairs, electromagnetic field has to rotate at $f_{\mathrm{e}} = 1333\,\mathrm{Hz}$, guaranteeing at most 15 switching periods over the course of one electrical revolution. Being delayed by k sampling periods causes an angular lag of

$$\Delta\theta_{\mathrm{e}} = k\omega_{\mathrm{e}}T_{\mathrm{s}} = 24^{\circ}, \qquad (4.23)$$
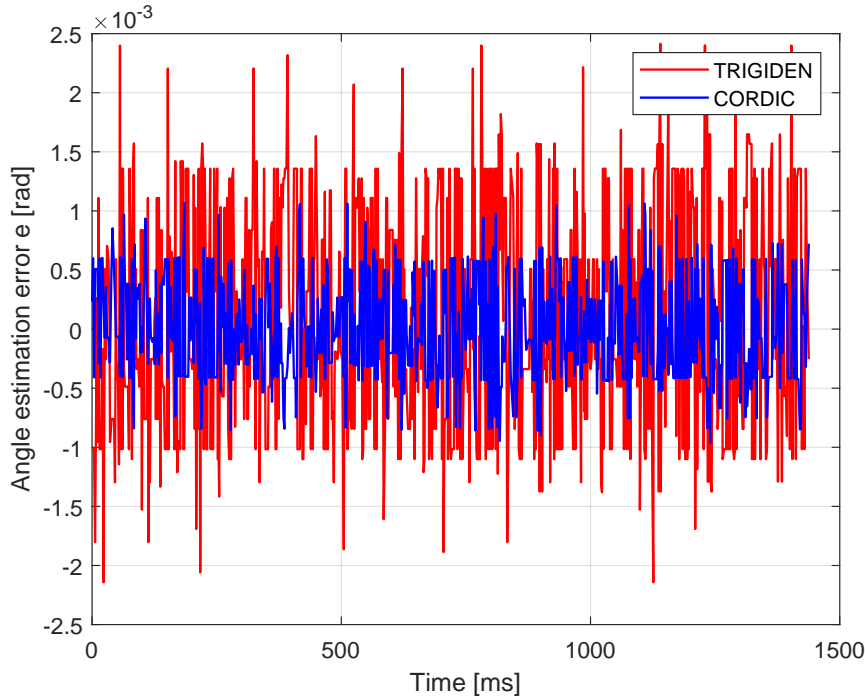
Figure 4.8: Comparison of observation error magnitude for both ATO architectures.

between the ideal synchronous frame of controlled machine and the synchronous frame used by the control algorithm. As a consequence, the Park transformation (2.8) computes incorrent *dq* currents.

Since the magnitude of error $\Delta\theta_e$ is directly proportional to the electrical angular frequency ω_e, even operation at lower speeds (say one quarter of maximal) suffers from performance and efficiency degradation, as the most integral principle of FOC – the effort to direct all[11] current into the *q* axis and none into the *d* axis for maximal torque operation – is violated.

A possible improvement is to use two angles in the control algorithm – first, the current angle $\theta_e(n)$ is used for forward Park transform, converting phase currents to *dq* reference frame, where the regulation designed in Chapter 5 takes place. Subsequently, a different angle – possibly the predicted $\theta_e(n+1)$ – could be used for the inverse Park transform. Due to limitations of testing equipment, achievable speeds were not high enough for angle leading to make any measurable difference.

---

[11]For the case of operation under base speed. Field weakening operation is not considered.
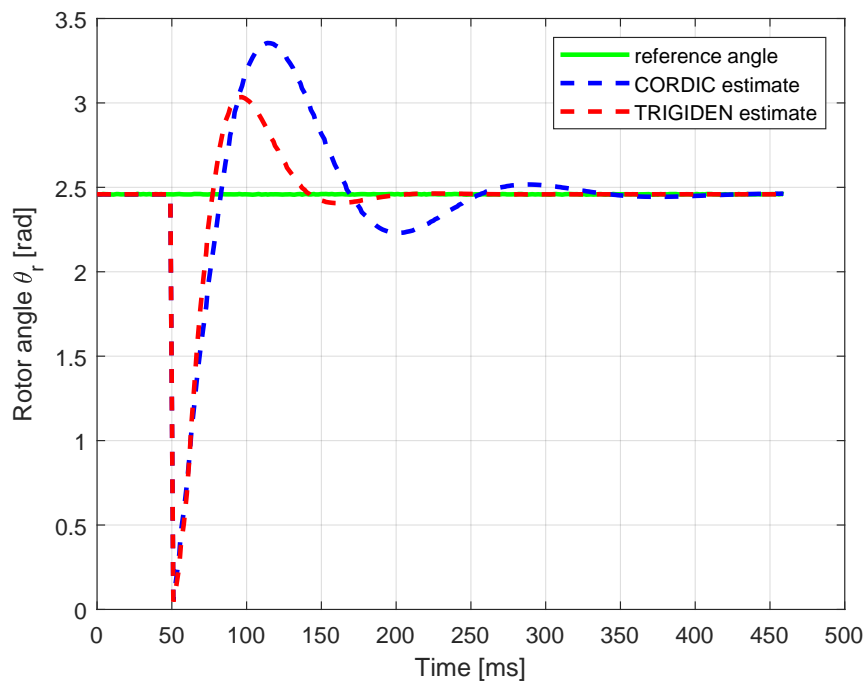
Figure 4.9: Step response of ATO.

Chapter 5

Controller design

This chapter analyzes various blocks constituting the FOC algorithm described in Section 3.1.3 from the perspective of the control theory. General design requirements are considered in order to plan appropriate regulator structure, for which tuning methods are researched to subsequently calculate controller gains. Although negative feedback is emphasized, options for feedforward compensation are investigated as well. Based on the discussion in Section 4.6, transport delays are neglected. Discretization of continuous-time regulators is considered in the end of this chapter.

5.1   DC link voltage compensation

Since switching MOSFET dynamics[1] are at least three orders of magnitude (1000 times) faster than electrical dynamics of the motor [52], [53], transistor half-bridge dynamics are completely neglected when considering the controller design. The rapid switching of half-bridge output between the positive and negative DC link rail with duty cycle DC and application of the volt-second principle described in Section 3.2 result in a transfer function

$$\frac{u}{DC} = U_{\text{DClink}}, \quad \text{where } DC \in [0, 1] \,, \tag{5.1}$$

of a variable gain, where u is the average output voltage.

In reality, the DC link voltage in an electric vehicle is not constant. The open-circuit voltage across battery terminals is an increasing function of its state-of-charge and hence gradually decreases as energy is expended. For the currently used accumulator, development of which is described in [54], a maximal voltage of 600 V drops to 432 V when discharged, resulting in a relative error of 28 % across the operating range when not compensated. Additionally, the accumulator internal resistance[2] and parasitic impedance of conductors cause a voltage drop proportional to instantaneous current. Both effects manifest as a multiplicative disturbance, causing the line to line

---

[1]Dynamics of switching elements are outside of this thesis scope, but are discussed in detail in [24]
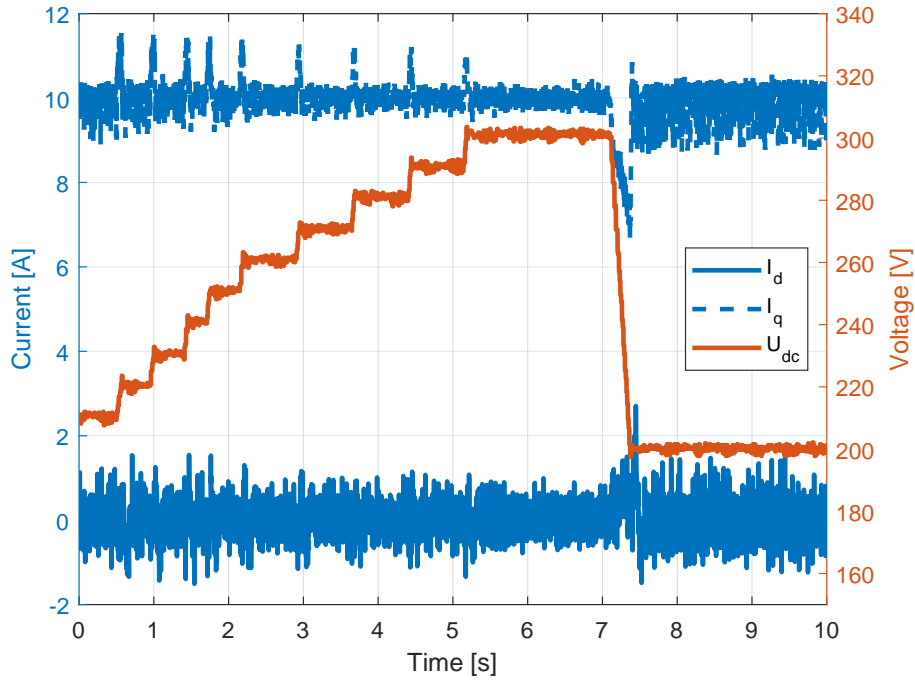
[2]estimated to be 220 mΩ in [54]

Figure 5.1: Current reference tracking with unregulated DC link voltage.

voltage applied to motor terminals to differ from the voltage commanded by current regulators.

Furthermore, [55] discusses the origination of additional current subharmonics due to the difference in frequencies of DC link fluctuation and inverter switching. These low-frequency components produce unpleasant audible noise and may excite vibrations through mechanical resonance.

Although DC link fluctuations are primarily a concern when the inverter is powered from rectified mains voltage, as is the case for railway traction among others, battery-powered automotive systems are not free of this problem either, e.g. due to the lack of synchronization between two adjacent motor controllers. From an economical standpoint, it is desirable to minimize the DC link capacity at the expense of greater fluctuations. Fluctuating DC link voltage may cause an undamped response or even instability of current control, as demonstrated in [13].

It is entirely possible to neglect all fluctuations and let the negative feedback take care of disturbance rejection at a cost of decreased dynamic performance. The controller will adjust the commanded duty cycle until measured currents match the setpoint. At that point, the controller output is no longer directly the voltage in *dq* reference frame, causing minor inconvenience in reasoning about the control structure. Significant transients in response to a step-like change of DC link voltage are shown in Figure 5.1. Alternatively, it is possible to close another loop around the half-bridge only, as proposed in [52]. The magnitude of phase voltages is normally not measured, therefore a set of

46

entirely new sensors would have to be added to the system. Although this approach may be appropriate for precise power supplies, it is not commonly used in motor control, where primarily machine currents are of interest.
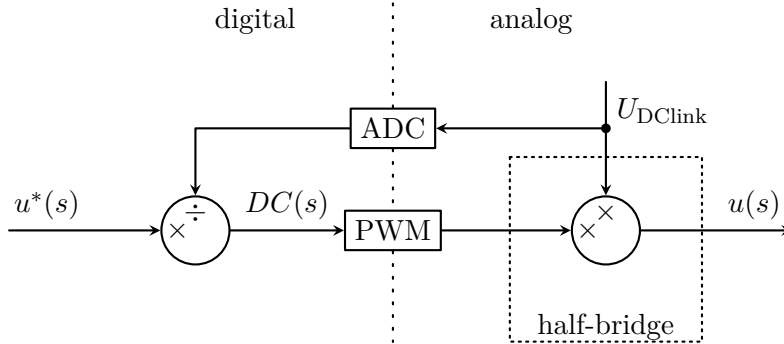

Figure 5.2: Structure of feedforward compensation of DC link voltage U_{DClink}.

Rather than closing an additional loop, this disturbance lends itself to an extremely easy measurement, thus a feedforward compensation may be considered [53]. Provided the immediate DC link voltage is available, it is possible to invert (5.1) and apply this gain on the output of current regulators, as illustrated in Figure 5.2. Gain of the transistor half-bridge is thus digitally cancelled and the system may be replaced with identity, not having to consider it anymore [4], [56]. This is confirmed by current waveforms displayed in Figure 5.3, where a sudden $100\,\text{V}$ step of U_{dc} has no direct effect on machine currents. Many further improvements of DC link fluctuation compensation are discussed in the literature, including predictors of periodic waveforms. An overview is offered in [57].

▊ **5.2 On model nonlinearity**

To review results derived in Section 2.2.5, specifically equation (2.26), the state-space model of PMSM in *dq* coordinates is

$$\frac{\mathrm{d}}{\mathrm{d}t} i_d = \frac{1}{L_d}(-R_d i_d + u_d + \omega_{\text{e}} L_q i_q), \tag{5.2a}$$

$$\frac{\mathrm{d}}{\mathrm{d}t} i_q = \frac{1}{L_q}(-R_q i_q + u_q - \omega_{\text{e}}(L_d i_d + \psi_{\text{M}})), \tag{5.2b}$$

where $u_{d,q}$ are two inputs and $i_{d,q}$ are states in the electrical domain. For now, consider ω_{e} a system state originating from the mechanical domain, although a state equation for $\frac{\mathrm{d}}{\mathrm{d}t}\omega_{\text{e}}$ is not explicitly listed. This decision will be later revisited.

The model is clearly non-linear for two reasons. First, the *q* axis equation (5.2b) contains a constant term $\omega_{\text{e}}\psi_{\text{M}}$. It could be eliminated by a simple change of variables. Second, both (5.2a) and (5.2b) contain coupling terms proportional to a product of the electrical angular frequency ω_{e} and a function of current in the other axis.
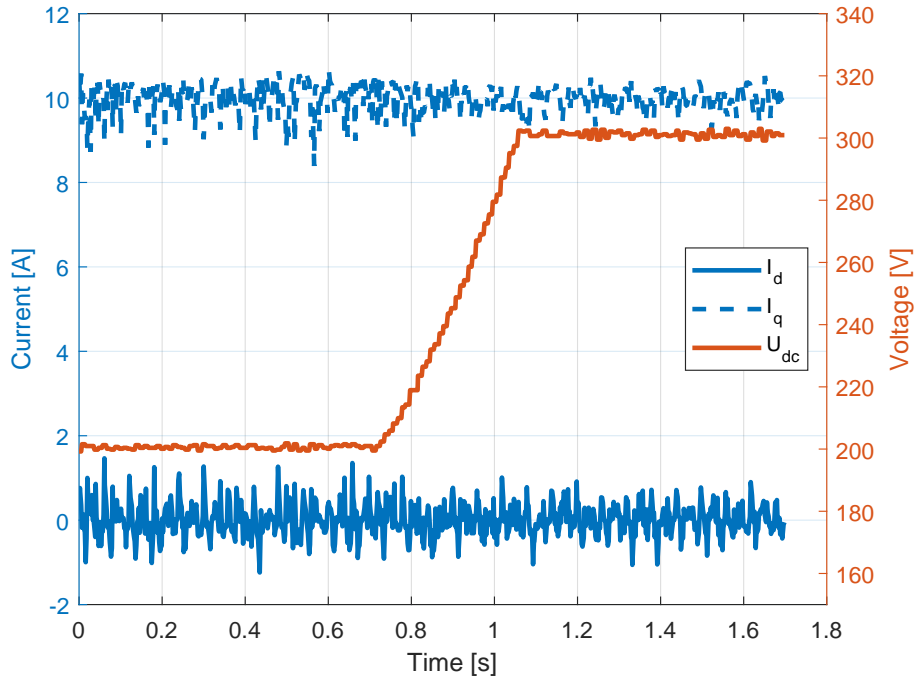
Figure 5.3: Current reference tracking with feedforward compensation of U_{dc}.

The non-linear state-space model (5.2) could be linearized around a specific operating point, forming matrices $\mathbf{A}$, $\mathbf{B}$, $\mathbf{C}$ and $\mathbf{D}$ from partial derivatives of equations (5.2) with respect to individual states and inputs. Considering the wide range of possible electrical speeds and currents, as stated in Section 1.2, the enormous size of the set of all relevant operating points – that is additionally dense in $\mathbb{R}^5$ – is apparent.

A trick suggested in [13] relies on linearization around the immediate setpoint. The linearization would be carried out symbolically in advance and used to derive closed-form expressions for regulator gains, suitable for programming into the microcontroller. Every time a new setpoint was received (approximately every 10 ms), the linearized model would be evaluated, recalculating regulator gains for subsequent control periods till the arrival of the new setpoint. An alternative solution is presented below.

▮ 5.3 System decoupling

Based on the discussion in Section 2.2.2, mechanical dynamics are significantly slower than current dynamics. So much so, ω_{e} may be removed from the state vector, and terms proportional to it in (5.2) may be interpreted as a control loop disturbance.

It is not unusual for industrial implementations to ignore this disturbance altogether, e.g. Texas Instruments [46], [58] or Microsemi [59]. This approach may be justified when using the PI regulator, in which case the open-loop
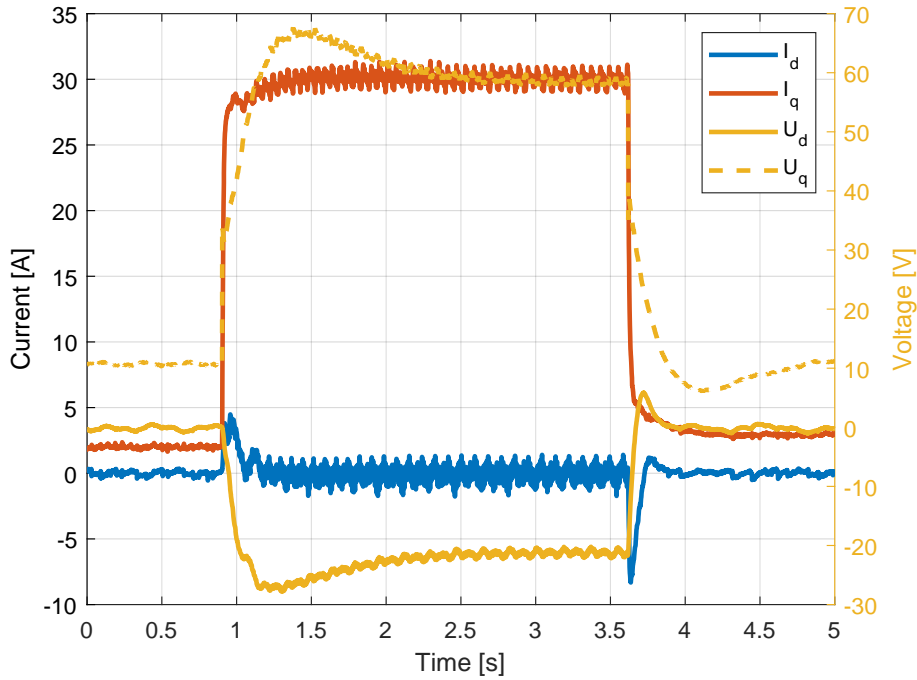
48

Figure 5.4: Response to a step-like change of setpoint without decoupling.

transfer function is a type one or more system, tracking a step-like reference with zero steady-state error even in the presence of a step-like disturbance [42]. Said vaguely, the negative feedback adjusts itself such that coupling terms proportional to ω_e – neglected in the model, but very present in the physical system – are compensated. Leaving aside, whether the disturbance really is step-like[3] and thus whether the current regulator is even able to compensate for it at all times, there are fundamental problems connected to the neglected dynamics. As pointed out in [60], ignoring the coupling terms leads to current spikes during transients, when each regulator has not only its own current to control, but must handle the inter-axis crosstalk due to the actions of the other regulator as well. This conclusion has been experimentally verified in a laboratory with the resulting waveforms depicted in Figure 5.4. Sudden change of setpoint i_q^* from 30 A to 3 A around time $t = 3.6\,\mathrm{s}$ causes a negative spike of i_d with magnitude 7 A.

It would be a missed opportunity, not to investigate the benefit of active decoupling, as proposed in [60], on system dynamics. Since the electrical angular frequency ω_e may be extracted as a side product of ATO operation, currents are system states and inductances in both axes are identified system parameters, the disturbance may be calculated and compensated in real-time. Using the structure displayed in Figure 5.5, the output $\vec{u}_\mathrm{fb}$ of feedback

---

[3]It clearly does not, because with piecewise constant torque – and hence current – setpoints, the angular acceleration is approximately constant and the speed changes almost linearly. Nevertheless, invoking the argument of significantly slower mechanical dynamics again, it may be concluded that at least partial disturbance rejection can be attained.
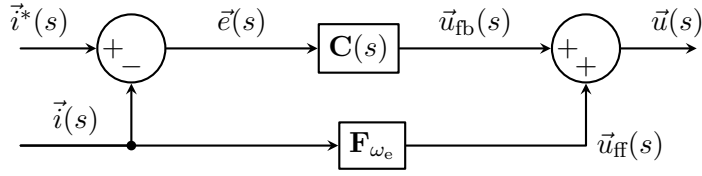
Figure 5.5: Feedforward decoupling compensator.
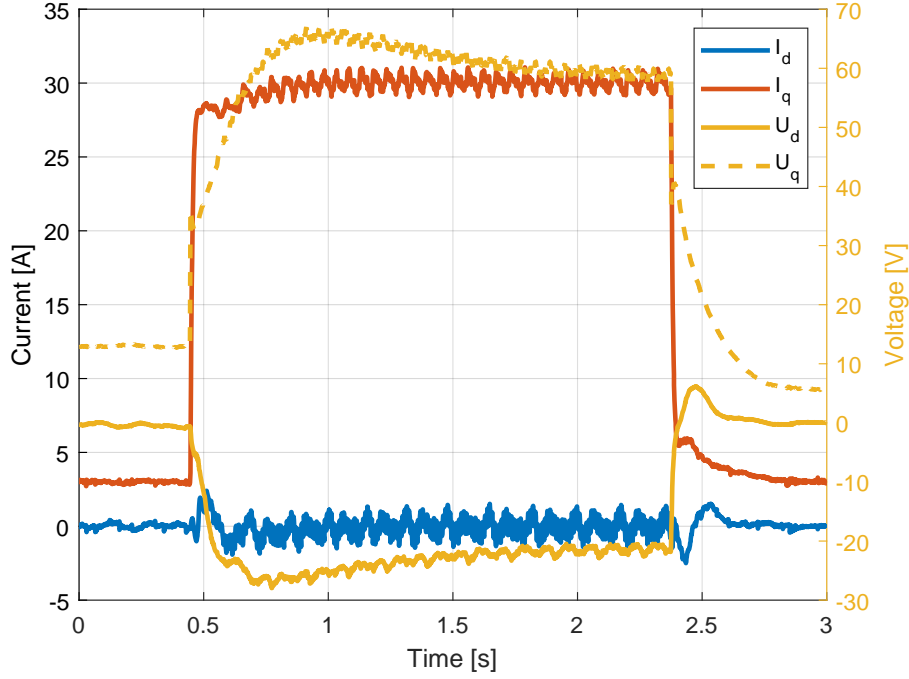
Figure 5.6: Response to a step-like change of reference with feedforward decoupling.

regulator $\mathbf{C}(s)$ is added to the output of the feedforward compensator

$$\vec{u}_{\text{ff}} = \mathbf{F}_{\omega_e}(\vec{i}) = \begin{bmatrix} 0 & -\omega_e L_q \\ \omega_e L_d & 0 \end{bmatrix} \cdot \vec{i} + \begin{bmatrix} 0 \\ \omega_e \psi_M \end{bmatrix}, \tag{5.3}$$

producing the vector of commanded voltages in the *dq* reference frame. Performance of second-order current loop with regulator (5.14) and feedforward axis decoupling is shown in Figure 5.6. The i_q^* current setpoint is changed from 3 A to 30 A at time $t \approx 450\,\text{ms}$ and then back to 3 A around $t \approx 2.4\,\text{s}$. Although some mutual influence is still noticeable with peak $i_d \approx 2\,\text{A}$, a significant improvement over Figure 5.4 has been achieved.

Another approach to machine axis decoupling is presented in [61], using different mathematical tools but arriving at similar results. The PMSM model (5.2) and current and voltage vectors in the *dq* reference frame are interpreted as complex numbers, deriving a transfer function with complex coefficients and designing a PI controller for it, such that dominant complex

poles of without complex conjugates are brought to the real axis.

The presented feedforward decoupling strategy is based solely on instantaneous values has been further improved in recent years. Authors of [62] mention possible instability in cases of extreme machine parameter variance, possible causes of which include magnetic asymmetry of the machine, the highly non-linear phenomenon of magnetic saturation or a distortion of the rotor magnetic field and are described in detail in [63]. Although it is simpler than feedback regulation, feedforward compensation has no way of accounting for parameter change. Hence alternative solutions have been proposed, including a pair of additional decoupling PI regulators, achieving significant robustness at a cost of decreased dynamic performance at low speeds.

Based on very positive results shown in Figure 5.6, the decoupling compensator (5.3) will be used, leaving two independent first-order LTI systems

$$
\begin{aligned}
\frac{\mathrm{d}}{\mathrm{d}t}i_d &= \frac{1}{L_d}(-R_d i_d + u_d), \\
\frac{\mathrm{d}}{\mathrm{d}t}i_q &= \frac{1}{L_q}(-R_q i_q + u_q),
\end{aligned}
\tag{5.4}
$$

to control. Follow-up work could consider some of the more advanced compensation techniques in case significant motor parameter variance is ever noticed.

5.4 PI regulator design
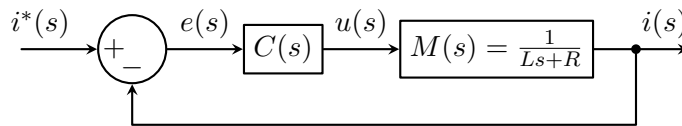
Figure 5.7: Closed-loop current control structure.

Assuming zero initial conditions, Laplace transform may be applied to (5.4) yielding the plant transfer function

$$
M(s) = \frac{i(s)}{u(s)} = \frac{1}{Ls + R}
\tag{5.5}
$$

symmetrical for both machine axes. Except for experiments with algorithms of modern control theory, such as model predictive control (MPC) or model reference adaptive control (MRAC), majority of industrial and academic motor control implementations rely nowadays upon the PI regulator either in parallel (5.6a) or in series (5.6b) form [64]. What various applications do not generally agree on is the calculation of regulator gains.

Manual PI tuning is always an option, using a wide variety of methods like the famous Ziegler-Nichols method[4], however it tends to deteriorate into

---

[4]Description of which is not given in thesis, but may be found in any control theory textbook, including [42], [43], [65]. Theoretical methods are prefered over more experimental ones.

a time consuming and tedious approach of trial and error, results of which are questionable. Finally, when automatic device commissioning outlined in Section 6.1 is desired, manual tuning becomes a significant hindrance.

5.4.1 Analytical PI tuning

Both PI structures

$$C_{\text{parallel}}(s) = K_p + \frac{K_i}{s},$$ (5.6a)

$$C_{\text{series}}(s) = K_a \left(1 + \frac{K_b}{s}\right),$$ (5.6b)

i.e. the parallel structure and the serial structure, respectivelly, are equivalent and – theoretically[5] – interchangeable with relations

$$K_a = K_p,$$
$$K_b = \frac{K_i}{K_p}.$$ (5.7)

Whereas in the parallel PI structure, K_p dominates the gain at higher frequencies and K_i influences the gain at lower frequencies, the series structure may be more intuitive to grasp because only K_a influences the gain and K_b is the regulator zero.

Many analytical PI(D) design procedures are discussed in [65], an overview of current controller tuning specifically is presented in [64]. Two methods have been tested and will be presented below, along with a performance evaluation based on experimental data from the implementation.

An attempt to completely cancel plant dynamics by inverting the plant transfer function (5.5) is destined to fail for both theoretical and practical reasons[6]. The simplest reasonable closed-loop structure is a first-order low-pass response

$$CL_{\text{desired}}(s) = \frac{\alpha}{s + \alpha}$$ (5.8)

with bandwidth α expressed in rad s^{-1} achieved by choosing [18]

$$K_a = L\alpha,$$
$$K_b = \frac{R}{L},$$ (5.9)

such that the regulator zero (ideally) cancels the plant pole. A first-order response guarantees stability and no overshoot, as is apparent from Figure 5.8. This choice of controller gains is actually a special case of the more general *Internal Model Controller* (IMC) PID proposed in [65] for the case of the first-order system with no transport delay.

---

[5]Practical implementations should consider e.g. the finite resolution caused by digital quantization such that precision is not lost in intermediate calculations. When an optimization method is used to tune the controller, it is possible that K_p becomes zero, leaving pure integral action, that can't be implemented using the series structure.

[6]Actual plant parameters will always differ slightly. Hence the cancellation will never be perfect. Furthermore, a more aggressive regulator requires a greater magnitude of the control signal, driving the system immediately into saturation.
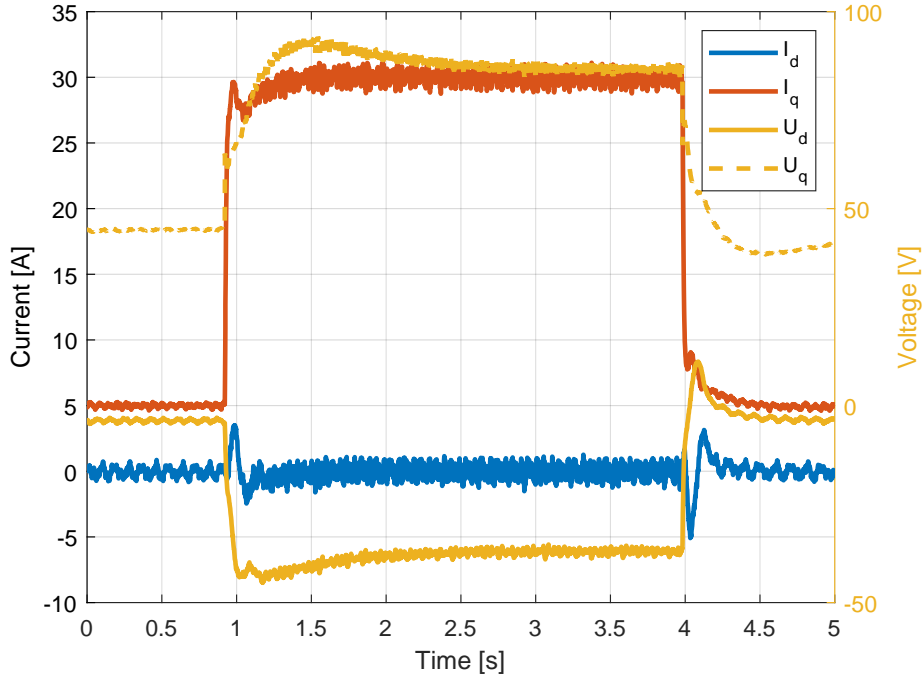
Figure 5.8: Step response of first-order closed current loop.

A second-order current loop calculated using the *pole placement* method is proposed in [66]. The closed-loop transfer function

$$CL(s) = \frac{M(s)C(s)}{1 + M(s)C(s)} \tag{5.10}$$

is written as a closed-form expression

$$CL(s) = \frac{\frac{K_p}{L}s + \frac{K_i}{L}}{s^2 + \frac{R+K_p}{L}s + \frac{K_i}{L}} \tag{5.11}$$

of controller gains and set equal to the desired transfer function $CL_{\mathrm{desired}}(s)$ found by considering closed-loop performance requirements either in the time or the frequency domain. Comparison of polynomials yields a system of (generally not necessarily linear) equations for individual coefficients. An alternative is to solve (5.10) for $C(s)$, yielding the appropriate regulator

$$C(s) = \frac{CL(s)}{M(s)(1 - CL(s))}, \tag{5.12}$$

capable of fulfilling the performance requirements.

Comparing the denominator of (5.11) to a general characteristic polynomial of a second-order system

$$p(s) = s^2 + 2\zeta\omega_{\mathrm{n}}s + \omega_{\mathrm{n}}^2 \tag{5.13}$$

53

with natural frequency ω_n and damping ratio ζ yields expressions for regulator gains

$$
\begin{aligned}
K_i &= L\omega_\mathrm{n}^2, \\
K_p &= 2\zeta\omega_\mathrm{n}L - R.
\end{aligned}
\tag{5.14}
$$

It should be noted that whereas the first-order current loop (5.9) posed no immediate threat of instability for any choice of reasonable[7] performance requirements, in the case of (5.14), choice of

$$
\omega_\mathrm{n}\zeta < \frac{R}{2L}
$$

results in a closed-loop zero in the right half-plane. A system with unstable zero no longer has minimum-phase property and as such manifests unwanted preshoot in the opposite direction when subject to a step-like reference.

According to [64], [67], a choice of $\zeta = 1/\sqrt{2}$, so-called *optimal damping*, is desirable in order to achieve the greatest disturbance rejection and speed without excessive peaking either in the time domain or in the Bode plot, achieving tolerable overshoot [43]

$$
OS = \exp\left(-\pi\frac{\zeta}{\sqrt{1-\zeta^2}}\right)
$$

less than 5 %. The natural frequency of the dominant pole pair may be calculated as a function [64]

$$
\omega_\mathrm{n} = \frac{\alpha}{\sqrt{1 - 2\zeta^2 + \sqrt{4\zeta^4 - 4\zeta^2 + 2}}}
\tag{5.15}
$$

of the required closed-loop bandwidth α. Design guidelines in [64] recommend target bandwidth lower than 30% or 17 % of the switching frequency for first-order (5.9) and second-order (5.14) current loops, respectively. This is clearly fulfilled in the case of $f_\mathrm{s} = 20\,\mathrm{kHz}$ switching frequency.

Actual closed-loop bandwidths were chosen to be $100\,\mathrm{rad\,s^{-1}}$ in order not to require an enormous amplitude of control signals. Step response of second-order current loop along with feedforward decoupling is shown in Figure 5.6.

It should be noted that (5.11) contains a stable zero. Depending on its position relative to the pair of poles, zero cancellation may be considered by adding a signal shaping filter with the transfer function

$$
D(s) = \frac{\frac{K_i}{L}}{\frac{K_p}{L}s + \frac{K_i}{L}}
\tag{5.16}
$$

on the reference path before the current loop, as illustrated in Figure 5.9.

---

[7]Reasonable performance requirements are not obviously incorrect. For example, neither negative bandwidth or time constant are considered reasonable.

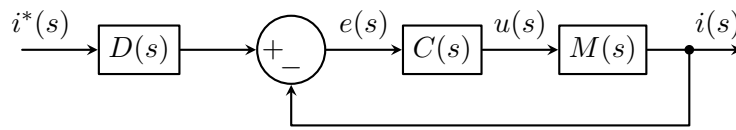**Figure 5.9:** Closed-loop control structure with added shaping filter.

▮ A note on discretization

An analytical discretization of the PI controller was shown in Section 4.4.3, results of which were used to implement proposed controllers on the hardware. Discretization of current regulators is even simpler due to the use of floating point number format, not requiring any additional scaling for the per unit system.

Chapter 6

System identification

Considering the non-linear motor model in state-space form from (2.26)

$$
\begin{aligned}
u_{\mathrm{d}} &= R_{\mathrm{d}} i_{\mathrm{d}} + L_{\mathrm{d}} \frac{\mathrm{d}}{\mathrm{d}t} i_{\mathrm{d}} - \omega_{\mathrm{e}} L_{\mathrm{q}} i_{\mathrm{q}}, \\
u_{\mathrm{q}} &= R_{\mathrm{q}} i_{\mathrm{q}} + L_{\mathrm{q}} \frac{\mathrm{d}}{\mathrm{d}t} i_{\mathrm{q}} + \omega_{\mathrm{e}} (L_{\mathrm{d}} i_{\mathrm{d}} + \psi_{\mathrm{M}}),
\end{aligned}
\tag{6.1}
$$

in the context of chosen control algorithms from Chapter 5, there are several blind spots to fill. The bare minimum is to identify machine inductances $L_{d,q}$ and resistances $R_{d,q}$ in both machine axes. When feedforward decoupling compensation (see Section 5.3) is employed, terms proportional to angular frequency ω_{e} must be evaluated, hence the magnetic flux ψ_{M} of PM must be known as well. In the affine conversion formula (4.5)

$$
\theta_{\mathrm{e}} = \frac{n_{\mathrm{p}}}{n_{\mathrm{r}}} (\theta_{\mathrm{r}} - \theta_{\mathrm{off}})
\tag{6.2}
$$

both the slope and the constant offset must be identified. This chapter discusses the motivation for, applicable methods of as well as the actual implementation of system identification. Online estimation methods are discussed briefly in the end of the chapter.

6.1 Automatic system identification

Although some system parameters may be extracted from the manufacturer's documentation, datasheets usually provide only typical values or a confidence interval bounded by minimal and maximal values guaranteed by design. Actual parameters will always differ slightly from one machine to another. Even worse, some parameters may not be listed at all. Motor datasheets usually include average winding resistance between machine terminals and inductance rather than "virtual" resistances and inductances in *dq* reference frame needed for motor model (6.1). Even if all required values were listed, it would still be beneficial to verify their correctness to rule out possible errors or device damage.

Manual system identification is a time consuming experimental process susceptible to human error, moreover it is not easily repeatable. State-of-the-art

parameter	symbol	value
winding resistance	R_s	$0.65\,\Omega$
d axis inductance	L_d	$5.4\,\mathrm{mH}$
q axis inductance	L_q	$7.6\,\mathrm{mH}$

Table 6.1: Parameters of UNIMOTOR 142UMD300CAAAA.

industrial control systems are therefore capable of *automatic commissioning* [68]. This process is usually comprised of two steps:

1. *system identification*, when a model of the controlled system is estimated from a series of tests, and

2. *controller auto-tuning*, when controller gains are calculated to meet closed-loop performance requirements.

Autocommissioning procedures are usually documented in the device manual, along with specific requirements of each test. As an example, it may be necessary to prevent the rotor from moving by fixing it mechanically in place. Individual tests may be dependent on each other, e.g. feedback sensor calibration has to precede inner loop tuning, which should in turn precede outer loop tuning, when a cascaded control structure is employed. Simple auto commissioning routines may be executed before each operation, compensating for the slow degradation of system parameters due to ageing. The benefits of automatic identification are further discussed in [69].

Inspiration has been taken from [68] for implementation of custom auto commissioning routines for the motor controller. Since three different motors were controlled when preparing this thesis, automated identification proved to be very beneficial, reducing the time required to transition from one machine to another. The following identification routines have been implemented in the motor controller firmware and tested in the laboratory environment:

- Resolver offset calibration calculates θ_off in (6.2), i.e. the distance from the resolver zero (mechanical angle at which $\theta_\mathrm{r} = 0$) to the direction of phase u (electrical angle $\theta_\mathrm{e} = 0$) (electrical zero).

- Calculation of motor to resolver pole ratio finds the conversion constant $n_\mathrm{p}/n_\mathrm{r}$ between electrical and mechanical angles and angular frequencies in (6.2).

- Estimation of motor parameters L and R from voltage step response with mechanically blocked rotor.

- Estimation of PM magnetic flux ψ_M from high-speed-low-torque operation.

Parameters of the PMSM used for testing are listed in Table 6.1.

■ **6.2** *LR* **estimation**

The motor controller applies a step of commanded voltage in either d or q axis whilst a mechanical brake prevents rotation. This ensures that $\omega_\mathrm{e} = 0$ and the coupling terms in (6.1) are eliminated, leaving only a simple first-order system. Samples of its step response are stored in internal memory and subsequently processed to obtain parameters R and L for the given axis. Since each identification lasts no more than half a second – and even then most of the time is spent by filtering and processing rather than the actual experiment because of very fast motor dynamics with the electrical time constant of several milliseconds – many successive cycles can be executed, averaging identified parameters.

Greater signal magnitudes are desirable, improving the signal to noise ratio. On the other hand, a current limit of 10 A was set for safety reasons, which, when exceeded, immediately disables all transistor driving complementary PWM outputs, forcing the current to flow through body diodes and slowly die down. This is safe since the blocked rotor prevents induction of any significant BEMF voltage.

A low pass digital filter was designed with Matlab *filterDesigner* tool to smoothen the current response, suppressing noise and extracting only valuable information without causing additional distortion. Since a typical electrical time constant of PMSM is in the order of lower milliseconds, $F_\mathrm{pass} = 100\,\mathrm{Hz}$ has been chosen to keep some safety margin. To achieve unity steady-state gain, required for precise estimation of motor resistance, maximal relative passband ripple Dpass = 0.001 was allowed. Stating general stopband parameters was more difficult – an effort was made to transfer full recorded motor response from the motor controller to the master computer and use the Fast Fourier Transform to estimate the noise frequency band, but due to technical limitations of the used toolchain, no useful representation in the master computer was obtained. An educated guess was made to choose the stopband one decade above the end of the passband with an additional margin of one octave. In summary, frequencies above 2 kHz were chosen to be attenuated.

A finite impulse response (FIR) filter was chosen for its linear phase property, delaying all frequency components by the same amount. This is important for compensation of any delays caused by postprocessing when estimating motor transport delay. The design tool is capable of converting the filter into a fixed point representation and printing a vector of coefficients. These coefficients can be directly copied into the C++ source code. At runtime, filter coefficients are loaded into the FMAC coprocessor and the filtering process is off-loaded from the CPU. Results of the simulation of this filter are depicted in Figure 6.1. Data tips show a delay of 0.5 ms, i.e. 10 sampling periods, exactly as expected from an FIR filter of order 20.
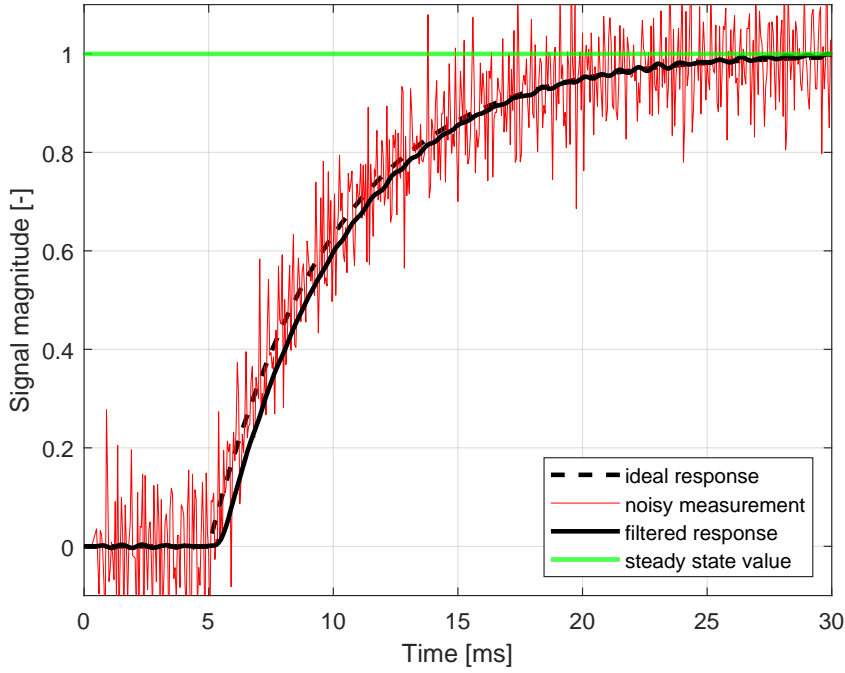
Figure 6.1: Filtering of motor's step response.

Applying the final value theorem[1]

$$\lim_{t \to \infty} y(t) = \lim_{s \to 0} sY(s)$$

on the Laplace transform

$$\mathcal{L}_-\{w(t)\} = \frac{1}{s}\frac{1}{Ls + R}$$

of plant's unit step response $w(t)$ yields the steady-state gain

$$w(t \to \infty) = \frac{1}{R}. \tag{6.3}$$

This result is expected, considering that the only current limiting element in the steady-state is the resistance of motor windings.

The expression for the system response

$$w(t) = \frac{1}{R}(1 - e^{-\frac{t}{\tau}}) \tag{6.4}$$

can be normalized to unity DC gain and solved for time t, yielding

$$t_{w\ \%} = -\tau \ln(1 - w). \tag{6.5}$$

The rise time

$$T_\mathrm{r} = t_{90\%} - t_{10\%} \tag{6.6}$$

---

[1]see e.g. [42]

59

is defined as the time required by the system response to rise from 90 % and 10 % of the steady-state value. Plugging (6.5) into (6.6) gives an expression for the time constant

$$\tau = \frac{T_\mathrm{r}}{-\ln 0.1 + \ln 0.9} \approx \frac{T_\mathrm{r}}{2.197} \tag{6.7}$$

in terms of rise time T_r, which lends itself to a comparably easier measurement from samples of the system response. Finally, the inductance L in the examined axis is determined as

$$\tau = \frac{L}{R} \quad \Rightarrow L = R\frac{T_\mathrm{r}}{2.197}. \tag{6.8}$$

The system transport delay T_d is estimated using the number of sampling periods elapsed from the step of u to the first sign of response from the system, when it crosses the level of 5 % of the steady-state value.

6.3 Resolver offset calibration

The motor can be aligned in a specific direction using open-loop control. By forcing voltages in the $\alpha\beta$ (stator) reference frame rather than the dq synchronous (rotor) frame, the stator magnetic field points in the desired direction and exerts torque force on the rotor, attempting to align it. Assuming the friction and other losses are negligible – which is not correct for a motor with some connected load or even the gearbox, but is satisfied without a connected load – the rotor aligns with the stator perfectly.

By commanding positive voltage in the α axis and zero in β, the rotor flux aligns with direction of stator winding U, i.e. the electrical zero $\theta_\mathrm{e} = 0$. From (6.2) follows that at that moment, the identified resolver offset is

$$\theta_\mathrm{off} = \theta_\mathrm{r}, \tag{6.9}$$

exactly the currently estimated resolver angle. This choice is not unique since more mechanical angles are aligned with the stator winding U due to relation (2.19).

6.4 Pole pair ratio calculation

This identification routine was implemented early in the motor controller design, primarily as a proof of concept and validation of coordinate transformations from Section 2.1 and modulation technique from Section 3.2. Based on the previous discussion in Section 2.2.4, it is self-evident that the the number of magnetic poles must be an even integer. Since it is an essential machine parameter, it is always listed in the datasheet, leaving no room for parameter uncertainty. Nevertheless, this routine has been preserved and may be useful in case of missing device documentation.

Open-loop control is used to estimate the ratio of motor pole pairs n_p to resolver pole pairs n_r. With no regards for the actual rotor angle, the stator magnetic field is slowly rotated by generating sinusoidal voltage setpoints in the $\alpha\beta$ frame. The magnetic field of the rotor is forced to rotate as well, generating sinusoidal waveforms on resolver outputs' envelopes.

After a fixed number of turns, the sinusoidal reference generator may be queried to attain the total electrical angle θ_e, whilst the angle tracking observer exposes information about the total resolver angle θ_r travelled. Plugging both values into (6.2) yields the constant of proportionality $\frac{n_p}{n_r}$. This identification procedure includes a check, whether both the motor, as well as the resolver, have the same notion of a positive direction of rotation.

▉ 6.5 PM flux ψ_M estimation

This identification method is a modification of the method presented in [70], refined for the environment and available tools. The motor is rotated by an external torque, e.g. a dynamo, at a steady speed. The feedforward compensation (5.3) is disabled and the current reference 0 A in both axes is set. When transients settle, the flowing current is close to zero, eliminating most of the terms in (6.1) and leaving only

$$u_q \approx \omega_e \psi_M. \tag{6.10}$$

To verify correctness, the motor BEMF constant K_{bemf} used as a constant of proportionality between electrical frequency and the the magnitude of induced voltage

$$u_{\text{RMS}} = K_{\text{bemf}} \omega_e, \tag{6.11}$$

ought to have – by definition – the same numeric value as ψ_M when coverted to SI units [60].

▉ 6.6 Online estimation methods

For various reasons, among which the thermal dependence of copper windings is the most intuitive, parameters of the motor are time-variant. In reality, self-inductances in both d and q axes, as well as the cross-coupling cinductance between axes, are nonlinear functions of load and even the instantaneous electrical angle. This is discussed in detail in [63], where, using the finite element method (FEM), inductance variance of up to 50% is observed for various operating points.

To achieve the highest possible accuracy of parameter identification in real-time, advanced online estimation methods are researched. For example in [71], a Model Reference Adaptive System (MRAS) approach is employed and elaborated on in detail including an improvement in combination with Particle Swarm Optimization (PSO). Although presented results show rapid convergence to about 1 % confidence interval around the real value of mechanical parameters J and b and even better accuracy for electrical parameters

(down to 0.1 % error of resistance estimate), this method is far from easy to implement in a real-time fashion on a microcontroller and has been deemed too difficult.

Other principles of online estimation exist, such as the one presented in [28]. It is based on (4.1), but used the other way around. Whereas for the sensorless operation, knowledge of $L_{d,q}$ is assumed and the electrical angle θ_e is extracted, in the case of online identification the known shaft angle is plugged into the impedance matrix, extracting components in the synchronous reference frame. In [72], two recursive parameter estimation methods are implemented and compared. First, the PMSM mathematical model is derived and discretized. It is subsequently converted into a linear regression optimization problem, which is solved either using the principle of least squares or an improvement in the form of Normalized Projection Algorithm (NPA). Although theoretical results are satisfactory, significant estimation errors are produced by the Simulink implementation.

Whereas the previously mentioned research attempts to devise a generic strategy free of any special assumptions for PMSM identification, an even simpler online estimation method based on solving (6.1) in the steady-state only is analyzed in [73]. In the steady-state, time derivatives are eliminated from the equation, leaving a system of two equations for four variables, which is clearly rank-deficient. Authors construct a second steady-state by temporarily moving a small step along the the curve of constant torque, preserving all mechanical properties, before returning back to the original operating point. Machine quantities sampled at both points are used to solve the system of equations, possibly in the sense of least squares if even more samples are used.

To name at least one example of an offline method, an *inductance-short circuit* method is discussed in [70]. The motor with open-loop between stator terminals is externally spun by another machine at steady speed, generating steady sinusoidal BEMF voltage. A short circuit of terminals causes current to flow. Equating the electrical and mechanical power, the winding resistance can be solved for. Even this first step is considered a weak point, since it does not account for mechanical losses in the gearbox. Furthermore, when preparing this thesis, a sufficiently precise source of mechanical power was not easily available, rendering this method inferior.

Chapter 7

Implementation on the hardware

7.1 ADC sampling times

Depending on the state of internal switch S, an internal sample and hold (S&H) capacitor C_{ADC} of an ADC is either following the input voltage (sampling stage) or holding the voltage stable for subsequent ADC circuitry to convert (hold stage).

During the sampling stage, voltage U_{ADC} across the S&H capacitor C_{ADC} is

$$U_{ADC}(t) = (U_{ADC}(\infty) - U_{ADC}(0))(1 - e^{\frac{-t}{\tau}}) + U_{ADC}(0), \qquad (7.1)$$

which is a typical response of a first-order system with time constant

$$\tau = (R_{ADC} + R_{EXT})C_{ADC}, \qquad (7.2)$$

where R_{ADC} is the combined resistance of ADC internals and R_{EXT} represents the internal resistance of source supplying the voltage to be measured. This time constant must be taken into account during system design.

In a practical application, the sampling stage must not require infinite time to properly measure the signal of interest. Optimal configuration takes the trade-off between accuracy and speed into account by

1. keeping the sampling time as long as possible to allow transients to settle, whilst simultaneously

2. limiting the sampling time to adhere to strict timing requirements of the motor control environment.

To assess whether all transients have properly settled, various thresholds are chosen depending on application's requirements. The usual rule of thumb involves waiting for 3τ or 5τ to elapse, resulting in a relative deviation from steady-state of 5 % or less than 1 % respectively, which is, however, insufficient for this design.

By the principle of analog to digital conversion, the input analog signal is inherently quantized[1]. As a consequence, when using N bits to represent full-scale range FS, each distinct digital word corresponds to an analog interval

---

[1] infinite resolution of magnitude is converted to finite resolution governed by the width of the used digital word

of width

$$\Delta y = \frac{FS}{2^N},$$ (7.3)

also known as one *least significant bit* (1 LSB). This observation offers a natural requirement for sufficient settling – allow enough time to pass such that the deviation from steady-state value is negligible in comparison to the quantization error.

To achieve settling to 1 LSB accuracy using 12-bit digital word, a total of

$$\frac{t_{\text{sampl}}}{\tau} = -\ln\left(\frac{1}{2^{12}}\right) \approx 8.32$$ (7.4)

time constants must elapse [74]. In practice, this duration is further extended to 9τ or more [75][76]. Using equations (7.2) and (7.4), ADC configuration could be formally calculated. Further theoretical analysis is however not possible as some parameters of the equivalent circuit are not documented by the manufacturer. Instead, only a table[2] of maximal permissible R_{AIN} as a function of used sampling time t_{sampl} is used to select the appropriate sampling time for each analog signal.

7.2 CORDIC

The *COordinate Rotation DIgital Computer*, abbreviated CORDIC, is a digital algorithm originally developed for trigonometric calculations. It is an iterative algorithm for approximation of scaled sine and cosine of an angle (conversion from polar to Cartesian coordinates), or of an angle and magnitude of a vector given by x and y coordinates. The algorithm converges to the exact solution linearly with the number of executed iterations using a principle similar to binary search. A detailed explanation of the algorithm is presented in [78].

---

[2]Table 67: *Maximum ADC R_{AIN}* in [77]

Chapter 8

Conclusions

In this thesis, software for a PMSM motor controller was designed. Individual building blocks were first analyzed theoretically based on research of state-of-the-art methods presented in published books and research papers. All parts then came together to compose a whole, creating a functional inverter capable of controlling PMSM of an electric vehicle. Due to constraints imposed by the available testing equipment, peak quantities achieved during testing were torque $T = 45\,\mathrm{N\,m}$, angular speed $n = 1500\,\mathrm{RPM}$ and power $P = 5.6\,\mathrm{kW}$. The observed behaviour of the control algorithm did not evince any indications of performance degradation, it is therefore expected to handle an even greater load.

Mathematical transformations derived using linear algebra in the beginning of Chapter 2 were subsequently employed in conjunction with fundamental physical principles to derive a mathematical model of PMSM in the dq reference frame rotating synchronously with the magnetic flux of permanent magnets by the end of Chapter 2.

Several automated identification routines have been proposed in Chapter 6 to estimate values of model parameters needed for the implementation of angle estimation and motor control methods. Using these routines, datasheet parameters of the used motor were verified.

The shaft angle sensing method described in Chapter 4 was successfully implemented in the digital domain, yielding reliable, accurate and noise-free estimates. Two methods have been implemented side by side and compared to demonstrate the power of trigonometric accelerator in the form of CORDIC coprocessor. Performance of method utilizing evaluation of `atan2` – normally computationally very demanding and therefore deemed unsuitable – was significantly improved, becoming a competitor to the more traditional method using the sum of angles identity for sine.

In Chapter 5, a system of feedback regulators and feedforward compensators was designed to meet the required closed-loop performance. Significant improvement in rejection of disturbance caused by the unregulated DC link voltage was demonstrated. Similarly, the mutual influence between both machine axes was successfully decreased by utilization of feedforward decoupling, as demonstrated on numerous system responses to various stimuli. Chapter 7 concluded the whole thesis with practical aspects of implementation

of previously discussed system blocks.

■ 8.1   Future work

There is more work to be done if the designed motor controller is to be employed in the upcoming race season 2022/2023. Field weakening is the most important missing block, as it is crucial for achieving high speed operation. It is also connected with a serious threat of damage or injury when mishandled, therefore its implementation was postponed, until the correctness of both the hardware as well as the control algorithm is proven through extensive testing.

Other paths, in this thesis explored only theoretically, include sensorless control or online machine parameter estimation. Modern control laws, such as model predictive control, could be considered as well, although methods of classical control theory were sufficient to achieve desired closed-loop behaviour.

Appendix A

Acronyms

A

ADC

    analog to digital converer. 2, 37, 42

ATO

    angle tracking observer. vi, 34, 38–44, 49

B

BEMF

    back electromotive force. 11, 15, 17, 19, 20, 29, 58, 61, 62

BLDC

    brushless DC motor. 15, 18

D

DOF

    degree of freedom. 5

DTC

    direct torque control. 21

E

EV

    electric vehicle. 20

F

FOC

    Field Oriented Control. 3, 20, 22, 29, 43, 45

I

IMD

insulation monitoring device. 10

L

LTI

linear time invariant. 51

P

PM

permanent magnet. 14, 16, 17, 56, 57

PMSM

permanent magnet synchronous motor. 1, 3, 5, 10, 14, 15, 17–19, 29, 47, 57, 62, 65

PWM

pulse width modulation. 22–25, 42

S

SiC

sillicon carbide. 2

V

VSI

voltage source inverter. vi, 22, 23

Appendix B

Bibliography

[1]   S. Tomášek, "Design of an electric powertrain for the formula student-class vehicle", Master's Thesis, Czech Technical University, Faculty of Electrical Engineering, Prague, 2019.

[2]   M. Kopiar, "Motor controller condifuration for use in electric formula powertrain", Bachelor's Thesis, Czech Technical University, Faculty of Electrical Engineering, Prague, 2021.

[3]   D. G. Holmes and T. A. Lipo, *Pulse Width Modulation For Power Converters, Principles and Practice* (IEEE Series on Power Engineering), M. E. El-Hawary, Ed. IEEE PRESS, 2003.

[4]   R. Krishnan, *Permanent Magnet Sysnchronous and Brushless DC Motor Drives.* CRC Press, 2010, ISBN: 978-0-8247-5384-9.

[5]   F. Rehm, P. Breining, S. Decker, J. Kolb, and M. Hiller, "Loss comparison of small delta- and star-connected permanent magnet synchronous machines", in *IECON 2019 - 45th Annual Conference of the IEEE Industrial Electronics Society*, vol. 1, 2019, pp. 1171–1176. DOI: 10.1109/IECON.2019.8927165.

[6]   F. J. T. E. Ferreira, "On the star, delta and star-delta stator winding connections tolerance to voltage unbalance", in *2015 IEEE International Electric Machines Drives Conference (IEMDC)*, 2015, pp. 1888–1894. DOI: 10.1109/IEMDC.2015.7409322.

[7]   J. Pyrhönen, V. Hrabovcová, and S. Semken, *Electrical machine drives control, an introduction*, 1st. Chichester, West Sussex: WILEY, 2016, ISBN: 978-111-9260-455.

[8]   P. Pillay and R. Krishnan, "Modeling, simulation, and analysis of permanent-magnet motor drives, Part i. the permanent-magnet synchronous motor drive", *IEEE Transactions on Industry Applications*, vol. 25, no. 2, pp. 265–273, 1989. DOI: 10.1109/28.25541.

[9]   N. Xu, H. Tong, Y. Jin, J. Xu, Z. Dai, and Y. Yang, "Sampling test and comparative analysis of insulation monitoring device in DC power system for station", in *2020 12th IEEE PES Asia-Pacific Power and Energy Engineering Conference (APPEEC)*, 2020, pp. 1–4. DOI: 10.1109/APPEEC48164.2020.9220540.

69

[10] J. Pyrhönen, V. Hrabovcová, and S. Semken, *Design of Rotating Electrical Machines*, 2nd. WILEY, 2013, ISBN: 978-1-118-58157-5.

[11] B. Drury, *The Control Techniques, Drives and Controls Handbook*, 2nd. London: The Institution of Engineering and Technology, 2009, ISBN: 978-1-84919-101-2.

[12] L. Werner, *Control of Electrical Drives*, 3rd. Springer, 2001, ISBN: 978-3-642-62609-8.

[13] O. Wallmark, S. Lundberg, and M. Bongiorno, "Input admittance expressions for field-oriented controlled salient PMSM drives", *IEEE Transactions on Power Electronics*, vol. 27, no. 3, pp. 1514–1520, 2012. DOI: 10.1109/TPEL.2011.2118231.

[14] J. F. Gieras, *Permanent Magnet Motor Technology*, 3rd, Ed. CRC Press, 2010.

[15] MathWorks. "Interior PMSM Matlab R2022a". (), [Online]. Available: https://uk.mathworks.com/help/mcb/ref/interiorpmsm.html.

[16] L. Chong, R. Dutta, and M. Rahman, "Application of concentrated windings in interior permanent magnet machine", in *2007 Australasian Universities Power Engineering Conference*, 2007, pp. 1–5. DOI: 10.1109/AUPEC.2007.4548069.

[17] B. Drury, *The Control Techniques, Drives and Controls Handbook*, 2nd. London: The Institution of Engineering and Technology, 2009, ISBN: 978-1-84919-101-2.

[18] X. Liu and A. J. Forsyth, "Active stabilisation of a PMSM drive system for aerospace applications", in *2008 IEEE Power Electronics Specialists Conference*, 2008, pp. 283–289. DOI: 10.1109/PESC.2008.4591942.

[19] J. M. Peña and E. V. Díaz, "Implementation of V/f scalar control for speed regulation of a three-phase induction motor", in *2016 IEEE ANDESCON*, 2016, pp. 1–4. DOI: 10.1109/ANDESCON.2016.7836196.

[20] P. K. Behera, M. K. Behera, and A. K. Sahoo, "Speed control of induction motor using scalar control technique", 2014.

[21] W. Tu, G. Xiao, C. Suo, and K. Yang, "A design of sensorless permanent magnet synchronous motor drive based on V/f control", in *2017 20th International Conference on Electrical Machines and Systems (ICEMS)*, 2017, pp. 1–5. DOI: 10.1109/ICEMS.2017.8056032.

[22] T. Zhang, B. Liu, and H. Zhang, "Direct torque control of permanent magnet synchronous motor", in *Proceedings of the 29th Chinese Control Conference*, 2010, pp. 3358–3361.

[23] Y.-S. Lai and J.-H. Chen, "A new approach to direct torque control of induction motor drives for constant inverter switching frequency and torque ripple reduction", *IEEE Transactions on Energy Conversion*, vol. 16, no. 3, pp. 220–227, 2001. DOI: 10.1109/60.937200.

[24]   B. J. Baliga, *Fundamentals of Power Semiconductor Devices*, 2nd, Ed. Springer, 2019, ISBN: 978-3-319-93987-2.

[25]   H. Pinheiro, F. Botteron, C. Rech, *et al.*, "Space vector modulation for voltage-source inverters: A unified approach", in *IEEE 2002 28th Annual Conference of the Industrial Electronics Society. IECON 02*, vol. 1, 2002, 23–29 vol.1. DOI: `10.1109/IECON.2002.1187476`.

[26]   J.-H. Youm and B.-H. Kwon, "An effective software implementation of the space-vector modulation", *IEEE Transactions on Industrial Electronics*, vol. 46, no. 4, pp. 866–868, 1999. DOI: `10.1109/TIE.1999.778263`.

[27]   S. Unal and M. Ozdemir, "Sensorless control of the permanent magnet synchronous motor using neural networks", in *2007 International Aegean Conference on Electrical Machines and Power Electronics*, 2007, pp. 638–642. DOI: `10.1109/ACEMP.2007.4510581`.

[28]   K. Scicluna, C. S. Staines, and R. Raute, "High frequency injection-based sensorless position estimation in permanent magnet synchronous machines", *Mathematics and Computers in Simulation*, vol. 184, pp. 137–152, 2021, ISSN: 0378-4754. DOI: `https://doi.org/10.1016/j.matcom.2020.02.024`. [Online]. Available: `https://www.sciencedirect.com/science/article/pii/S037847542030063X`.

[29]   D. Stanica, N. Bizon, and M. Arva, "A brief review of sensorless AC motors control", in *2021 13th International Conference on Electronics, Computers and Artificial Intelligence (ECAI)*, 2021, pp. 1–7. DOI: `10.1109/ECAI52376.2021.9515049`.

[30]   D. Xu, B. Wang, G. Zhang, G. Wang, and Y. Yu, "A review of sensorless control methods for ac motor drives", *CES Transactions on Electrical Machines and Systems*, vol. 2, no. 1, pp. 104–115, 2018. DOI: `10.23919/TEMS.2018.8326456`.

[31]   G. Wang, G. Zhang, and D. Xu, *Position sensorless control techniques for permanent magnet synchronous machine drives*. Singapore: Springer, 2020, ISBN: 978-981-15-0049-7.

[32]   W. Commons, *File:quadrature diagram.svg — wikimedia commons, the free media repository*, [Online; accessed 19-May-2022], 2020. [Online]. Available: `%5Curl%7Bhttps://commons.wikimedia.org/w/index.php?title=File:Quadrature_Diagram.svg&oldid=456640418%7D`.

[33]   *White paper: The basics of how an encoder works*, 10/09/20, ENCODER Products Company, 2019.

[34]   *Fast and simple measurement of position changes*, iC-Haus GmbH, 2012. [Online]. Available: `https://www.ichaus.de/upload/pdf/WP2en_EncoderInterface_14082012.pdf`.

[35]   *White paper: Noise and signal distortion considerations, For encoders in motion control applications*, 11/5/19, ENCODER Products Company, 2019.

[36]   *White paper: Accuracy of encoders*, 11/22/19, ENCODER Products Company, 2019.

[37]   L. Chalupa, "An overview of the resolver interface for motor control applications", Freescale semiconductors, Tech. Rep., 2014.

[38]   A. Kaewpoonsuk, R. Katman, T. Kamsri, A. Rerkratn, and V. Riewruja, "A simple amplitude detector-based demodulator for resolver converters", in *ICCAS 2010*, 2010, pp. 370–373. DOI: `10.1109/ICCAS.2010.5670163`.

[39]   M. Benammar, L. Ben-Brahim, and M. Alhamadi, "A novel resolver-to-360° linearized converter", *IEEE Sensors Journal*, vol. 4, no. 1, pp. 96–101, 2004. DOI: `10.1109/JSEN.2003.820317`.

[40]   X. Yongxiang, Z. Dianchen, W. Yanyu, Z. Jibin, and S. Jing, "DSP based all-digital resolver-to-digital conversion using DSRF-PLL", in *Proceedings of The 7th International Power Electronics and Motion Control Conference*, vol. 2, 2012, pp. 1210–1215. DOI: `10.1109/IPEMC.2012.6259008`.

[41]   A. Bunte and S. Beineke, "High-performance speed measurement by suppression of systematic resolver and encoder errors", *IEEE Transactions on Industrial Electronics*, vol. 51, no. 1, pp. 49–53, 2004. DOI: `10.1109/TIE.2003.822084`.

[42]   G. F. Franklin, J. D. Powell, and A. Emami-Naeini, *Feedback Control of Dynamic Systems*, global, 7th. Pearson, 2015, ISBN: 1-29-206890-6.

[43]   R. C. Dort and R. H. Bishop, *Modern control systems*, 13th. Pearson, 2017, ISBN: 978-0-13-440762-3.

[44]   L. Huan and W. Zhong, "On estimation algorithm of angular velocity for servo motors with resolvers", in *2018 Chinese Control And Decision Conference (CCDC)*, 2018, pp. 4019–4024. DOI: `10.1109/CCDC.2018.8407821`.

[45]   H. Liu and Z. Wu, "Demodulation of angular position and velocity from resolver signals via Chebyshev filter-based type III phase locked loop", *Electronics*, vol. 7, no. 12, 2018, ISSN: 2079-9292. DOI: `10.3390/electronics7120354`. [Online]. Available: `https://www.mdpi.com/2079-9292/7/12/354`.

[46]   S. Erwan, "Application report SPRA5888, Implementation of a speed field oriented control of 3-phase PMSM motor using TMS320F240", Texas Instruments, Tech. Rep., 1999.

[47]   Y. Chen and Y. Tsividis, "Design considerations for variable-rate digital signal processing", in *2016 IEEE International Symposium on Circuits and Systems (ISCAS)*, 2016, pp. 2479–2482. DOI: `10.1109/ISCAS.2016.7539095`.

[48]   F. J. Galindo Guarch, P. Baudrenghien, and J. M. Moreno Arostegui, "An architecture for real-time arbitrary and variable sampling rate conversion with application to the processing of harmonic signals", *IEEE Transactions on Circuits and Systems I: Regular Papers*, vol. 67, no. 5, pp. 1653–1666, 2020. DOI: `10.1109/TCSI.2019.2960686`.

[49]   B.-H. Bae and S.-K. Sul, "A compensation method for time delay of full-digital synchronous frame current regulator of PWM AC drives", *IEEE Transactions on Industry Applications*, vol. 39, no. 3, pp. 802–810, 2003. DOI: `10.1109/TIA.2003.810660`.

[50]   J. Guo, T. Fan, Q. Li, and X. Wen, "Coupling and digital control delays affected stability analysis of permanent magnet synchronous motor current loop control", in *2019 IEEE Vehicle Power and Propulsion Conference (VPPC)*, 2019, pp. 1–5. DOI: `10.1109/VPPC46532.2019.8952510`.

[51]   M. Nicola, C.-I. Nicola, and M. Duţă, "Delay compensation in the PMSM control by using a smith predictor", in *2019 8th International Conference on Modern Power Systems (MPS)*, 2019, pp. 1–6. DOI: `10.1109/MPS.2019.8759752`.

[52]   M. C. Trigg, H. Dehbonei, and C. V. Nayar, "DC bus compensation for a sinusoidal voltage source inverter with wave-shaping control", in *IECON 2006 - 32nd Annual Conference on IEEE Industrial Electronics*, 2006, pp. 2832–2837. DOI: `10.1109/IECON.2006.347992`.

[53]   M. Ryan and R. Lorenz, "A high performance sine wave inverter controller with capacitor current feedback and "back-emf" decoupling", in *Proceedings of PESC '95 - Power Electronics Specialist Conference*, vol. 1, 1995, 507–513 vol.1. DOI: `10.1109/PESC.1995.474857`.

[54]   P. Hainc, "Návrh elektroniky pro akumulátorovou baterii elektromobilu", Master's Thesis, Czech Technical University, Faculty of Electrical Engineering, Prague, 2021.

[55]   Z. Salam and C. Goodman, "Compensation of fluctuating dc link voltage for traction inverter drive", in *1996 Sixth International Conference on Power Electronics and Variable Speed Drives (Conf. Publ. No. 429)*, 1996, pp. 390–395. DOI: `10.1049/cp:19960946`.

[56]   M. Ryan, W. Brumsickle, and R. Lorenz, "Control topology options for single-phase ups inverters", *IEEE Transactions on Industry Applications*, vol. 33, no. 2, pp. 493–501, 1997. DOI: `10.1109/28.568015`.

[57]   S. Zhao, X. Huang, Y. Fang, and J. Zhang, "Compensation of dc-link voltage fluctuation for railway traction PMSM in multiple low-switching-frequency synchronous space vector modulation modes", *IEEE Transactions on Vehicular Technology*, vol. 67, no. 1, pp. 235–250, 2018. DOI: `10.1109/TVT.2017.2765000`.

[58]   B. Akin and M. Bhardwaj, "Application report SPRABP8, Sensored field oriented control of 3-phase induction motors", Texas Instruments, Tech. Rep., 2013.

[59] *Field oriented control of permanent magnet synchronous motors, User's guide*, Rev 0, Microsemi, 2021.

[60] A. Zentai and T. Daboczi, "Improving motor current control using decoupling technique", in *EUROCON 2005 - The International Conference on "Computer as a Tool"*, vol. 1, 2005, pp. 354–357. DOI: 10.1109/EURCON.2005.1629934.

[61] F. Briz, M. Degner, and R. Lorenz, "Analysis and design of current regulators using complex vectors", *IEEE Transactions on Industry Applications*, vol. 36, no. 3, pp. 817–825, 2000. DOI: 10.1109/28.845057.

[62] K. Lee and J.-I. Ha, "Dynamic decoupling control method for PMSM drive with cross-coupling inductances", in *2017 IEEE Applied Power Electronics Conference and Exposition (APEC)*, 2017, pp. 563–569. DOI: 10.1109/APEC.2017.7930750.

[63] K. Lee, J.-I. Ha, and D. Simili, "Decoupled current control with novel anti-windup for PMSM drives", in *2017 IEEE Energy Conversion Congress and Exposition (ECCE)*, 2017, pp. 1183–1190. DOI: 10.1109/ECCE.2017.8095923.

[64] A. M. Diab, S. Bozhko, F. Guo, *et al.*, "Fast and simple tuning rules of synchronous reference frame proportional-integral current controller", *IEEE Access*, vol. 9, pp. 22 156–22 170, 2021. DOI: 10.1109/ACCESS.2021.3054845.

[65] A. Astöm and T. Hägglund, *PID Controllers, Theory, design, and tuning*, 2nd ed. Instrument Society of America, 1994, ISBN: 1-55617-516-7.

[66] *An4642, Motor control application tuning (MCAT) tool for 3-phase PMSM*, Rev 1, Freescale Semiconductor, 2013.

[67] C. H. Van Der Broeck, S. A. Richter, J. V. Bloh, and R. W. De Doncker, "Methodology for analysis and design of discrete time current controllers for three-phase PWM converters", *CPSS Transactions on Power Electronics and Applications*, vol. 3, no. 3, pp. 254–264, 2018. DOI: 10.24295/CPSSTPEA.2018.00025.

[68] *Commissioning and tuning guide*, version 4.20.9, Synapticon GmbH, 2022. [Online]. Available: https://doc.synapticon.com/oblac_drives/Synapticon_Commissioning_and_Tuning_Guide.pdf.

[69] X. Cheng, S. Zhang, Y. Chen, H. Zhang, and XuZhu, "Auto-commissioning and adaptive tuning of servo control parameters in an electro-hydraulic system based on physical plant model", in *2014 IEEE 15th Workshop on Control and Modeling for Power Electronics (COMPEL)*, 2014, pp. 1–5. DOI: 10.1109/COMPEL.2014.6877172.

[70] A. Gebregergis, M. Islam, T. Sebastian, and R. Ramakrishnan, "Evaluation of inductance in a permanent magnet synchronous motor", in *2011 IEEE International Electric Machines Drives Conference (IEMDC)*, 2011, pp. 1171–1176. DOI: `10.1109/IEMDC.2011.5994768`.

[71] G. Su, P. Wang, Y. Guo, G. Cheng, S. Wang, and D. Zhao, "Multiparameter identification of permanent magnet synchronous motor based on model reference adaptive system—simulated annealing particle swarm optimization algorithm", *Electronics*, vol. 11, p. 159, Jan. 2022. DOI: `10.3390/electronics11010159`.

[72] H. Neugebauer, "Parameter identification of a permanent magnet sysnchronous motor", Master's Thesis, Chalmers University of Technology, Gothenburg, Sweden, 2012.

[73] M. Zhou, L. Jiang, and C. Wang, "Real-time multiparameter identification of a salient-pole PMSM based on two steady states", *Energies*, vol. 13, no. 22, 2020, ISSN: 1996-1073. DOI: `10.3390/en13226109`. [Online]. Available: `https://www.mdpi.com/1996-1073/13/22/6109`.

[74] *Application note AN5250, How to increase the analog-to-digital converter accuracy in an application*, Rev 0, Freescale Semiconductor, Inc., 2016.

[75] R. Pavlanin, *An4373: Cookbook for SAR ADC measurements, ADC measurements done properly*, Rev 1, Freescale Semiconductor, Inc., 2014.

[76] *Application note AN2834, How to get the best adc accuracy in STM32 microcontrollers*, Rev 8, ST Microelectronics, 2022.

[77] *Ds12288, STM32G474xB, STM32G474xC, STM32G474xE datasheet*, Rev 6, ST Microelectronics, 2021.

[78] J. E. Volder, "The CORDIC trigonometric computing technique", *IRE Transactions on Electronic Computers*, vol. EC-8, no. 3, pp. 330–334, 1959. DOI: `10.1109/TEC.1959.5222693`.

75